Phagocytic glia are obligatory intermediates in transmission of mutant huntingtin aggregates across neuronal synapses

Kirby M. Donnelly[1], Olivia R. DeLorenzo[2], Wint M. Thu[1], Gabrielle E. Pisano[1], Liqun Luo[3,4], Ron R. Kopito[3], Margaret M. Panning Pearce[1,2,5]

[1]Department of Biological Sciences and [2]Program in Neuroscience, University of the Sciences, Philadelphia, PA 19063, USA

[3]Department of Biology, Stanford University, Stanford, CA 94305, USA

[4]Howard Hughes Medical Institute, Stanford University, Stanford, CA 94305, USA

[5]Correspondence: m.pearce@usciences.edu

ABSTRACT

Emerging evidence supports the hypothesis that pathogenic protein aggregates associated with many neurodegenerative diseases spread from cell to cell through the brain in a manner akin to infectious prions. Here, we show that mutant huntingtin (mHtt) aggregates associated with Huntington disease transfer anterogradely from presynaptic to postsynaptic neurons in the adult *Drosophila* olfactory system. Trans-synaptic transmission of mHtt aggregates is inversely correlated with neuronal activity and blocked by caspase inhibition in presynaptic neurons, implicating synaptic dysfunction and cell death in aggregate spreading. Remarkably, mHtt aggregate transmission across synapses requires the scavenger receptor Draper and involves a transient visit to the glial cytoplasm, indicating that phagocytic glia act as obligatory intermediates in aggregate spreading between synaptically-connected neurons. These findings expand our understanding of phagocytic glia as double-edged players in neurodegeneration—they clear neurotoxic protein aggregates, but also provide opportunities for prion-like seeds to evade phagolysosomal degradation and propagate further in the brain.

INTRODUCTION

Neurodegenerative diseases have emerged as one of the greatest healthcare challenges in our aging society, and thus a better understanding the underlying pathological mechanisms is critical to development of more effective therapies or cures for these fatal disorders. A common molecular feature of many neurodegenerative diseases [e.g., Alzheimer disease (AD), frontotemporal dementias (FTD), Parkinson disease (PD), amyotrophic lateral sclerosis (ALS), and Huntington disease (HD)] is the misfolding of certain proteins, driving their accumulation into insoluble, amyloid aggregates (Knowles et al., 2014). Appearance of proteinaceous deposits in patient brains correlates closely with neuronal loss and clinical progression, and strategies to lower production or enhance clearance of pathological proteins in the degenerating brain have shown therapeutic promise in animal models and clinical trials (Boland et al., 2018; Li et al., 2019; Tabrizi et al., 2019).

Post-mortem histopathological analyses (Braak and Braak, 1991; Braak et al., 2003; Brettschneider et al., 2013) and *in vivo* imaging studies (Deng et al., 2004; Poudel et al., 2019) indicate that proteopathic lesions associated with neurodegeneration appear in highly-reproducible and disease-specific spatiotemporal patterns through the brain. Interestingly, these patterns largely follow neuroanatomical tracts (Ahmed et al., 2014; Mezias et al., 2017), suggesting a central role for synaptic connectivity in pathological aggregate spreading. Accumulating evidence supports the idea that intracellular aggregates formed by tau, α-synuclein, TDP-43, SOD1, and mutant huntingtin (mHtt) transfer from cell-to-cell and self-replicate by recruiting natively-folded versions of the same protein, analogous to how infectious prion protein (PrP^{Sc}) templates the conformational change of soluble PrP^{C} in prion diseases (Vaquer-Alicea and Diamond, 2019). Numerous studies have pointed to roles for endocytosis and exocytosis (Asai et al., 2015; Babcock and Ganetzky, 2015; Chen et al., 2019; Holmes et al., 2013; Lee et al., 2010; Zeineddine et al., 2015), membrane permeabilization (Chen et al., 2019; Falcon et al., 2018; Flavin et al., 2017; Zeineddine et al., 2015), tunneling nanotubes (Costanzo et al., 2013; Sharma and Subramaniam, 2019), and neuronal activity (Wu et al., 2016) in entry and/or exit of pathogenic protein assemblies from cells, but the exact mechanisms by which amyloid aggregates or

53 on-pathway intermediates could cross one or more biological membranes in the highly complex central
54 nervous system (CNS) remain an enigma.

55 Glia are resident immune cells of the CNS, constantly surveying the brain to maintain
56 homeostasis and to respond rapidly to tissue damage or trauma. Reactive astrocytes and microglia
57 provide a first line of defense in neurodegeneration by infiltrating sites of neuronal injury, upregulating
58 immune-responsive genes, and phagocytosing dying neurons and other debris, including protein
59 aggregates (Asai et al., 2015; Grathwohl et al., 2009; Wyss-Coray et al., 2003). Prolonged activation of
60 these glial responses results in chronic inflammation, exacerbating synaptic dysfunction and neuronal
61 loss (Hammond et al., 2018). We and others have previously shown that Draper, a *Drosophila*
62 scavenger receptor responsible for recognizing and phagocytosing cellular debris (Freeman, 2015),
63 regulates the load of mHtt (Pearce et al., 2015) and $A\beta_{1-42}$ (Ray et al., 2017) aggregate pathology in the
64 fly CNS. Remarkably, we also found that a portion of phagocytosed neuronal mHtt aggregates gain
65 entry into the glial cytoplasm and there nucleate the aggregation of normally-soluble wild-type Htt
66 (wtHtt) proteins, suggesting that glial phagocytosis provides a route for spreading of prion-like
67 aggregates in intact brains. Consistent with our results, microglial ablation suppresses pathological tau
68 transmission between synaptically-connected regions of the mouse brain (Asai et al., 2015), and PrP^{Sc}
69 transfers from infected astrocytes to co-cultured neurons (Victoria et al., 2016). Thus, these findings
70 suggest that phagocytic glia could play double-edged roles in neurodegeneration, with normally
71 neuroprotective clearance mechanisms contributing to dissemination of prion-like aggregate species
72 through the CNS.

73 A plethora of studies from the last decade have strengthened the prion-like hypothesis for
74 neurodegenerative diseases, but we still lack a clear understanding of how pathogenic protein
75 aggregates spread in an intact CNS. In this study, we adapted our previously-described *Drosophila* HD
76 model to examine roles for synaptic connectivity and phagocytic glia in prion-like mHtt aggregate
77 transmission in the fly CNS. HD is an autosomal dominant disorder caused by expansion of a CAG
78 repeat region in exon 1 of the Htt gene, resulting in production of highly aggregation-prone mHtt
79 proteins containing abnormally expanded polyglutamine (polyQ≥37) tracts (Bates et al., 2015;

80 MacDonald et al., 1993). By contrast, wtHtt proteins containing polyQ≤36 tracts only aggregate upon
81 nucleation by pre-formed Htt aggregate “seeds” (Chen et al., 2001; Preisinger et al., 1999). A growing
82 body of evidence from cell culture (Chen et al., 2001; Costanzo et al., 2013; Holmes et al., 2013; Ren et
83 al., 2009; Sharma and Subramaniam, 2019; Trevino et al., 2012) and *in vivo* (Ast et al., 2018; Babcock
84 and Ganetzky, 2015; Jeon et al., 2016; Masnata et al., 2019; Pearce et al., 2015; Pecho-Vrieseling et
85 al., 2014) models of HD supports the idea that pathogenic mHtt aggregates have prion-like properties—
86 they transfer from cell to cell and template the conformational change of soluble wtHtt proteins. Here,
87 we report that mHtt aggregates formed in presynaptic olfactory receptor neuron (ORN) axons effect
88 prion-like conversion of wtHtt proteins expressed in the cytoplasm of their postsynaptic partner
89 projection neurons (PNs) in the adult fly olfactory system. Remarkably, we find that transfer of mHtt
90 aggregates from presynaptic ORNs to postsynaptic PNs was abolished in Draper-deficient animals and
91 requires passage of the aggregate seeds through the cytoplasm of Draper-dependent glial cells.
92 Together, these findings support the conclusion that phagocytic glia are obligatory intermediates in
93 prion-like transmission of mHtt aggregates between synaptically-connected neurons *in vivo*.

RESULTS

Anterograde transfer of prion-like mHtt aggregates across synapses in the adult fly olfactory system

Aggregates formed by N-terminal fragments of mHtt generated by aberrant splicing (e.g., exon 1; Htt_{ex1}) (Sathasivam et al., 2013) or caspase cleavage (e.g., exon 1-12; Htt_{ex1-12}) (Graham et al., 2006) (Fig. 1A) accumulate in HD patient brains, are highly cytotoxic, and spread between cells in culture and *in vivo* (Babcock and Ganetzky, 2015; Costanzo et al., 2013; Pearce et al., 2015; Pecho-Vrieseling et al., 2014; Ren et al., 2009). We have previously established transgenic *Drosophila* that employ binary expression systems [e.g., Gal4-UAS, QF-QUAS, or LexA-LexAop (Riabinina and Potter, 2016)] to express fluorescent protein (FP) fusions of Htt_{ex1} in non-overlapping cell populations in order to monitor cell-to-cell transfer of $mHtt_{ex1}$ aggregates in intact brains (Donnelly and Pearce, 2018; Pearce et al., 2015). Our experimental approach (Fig. 1B) exploits the fact that $wtHtt_{ex1}$ proteins only aggregate upon encountering $mHtt_{ex1}$ aggregate seeds (Chen et al., 2001; Preisinger et al., 1999), such that transfer of $mHtt_{ex1}$ aggregates from “donor” cells is reported by conversion of cytoplasmic $wtHtt_{ex1}$ from its normally soluble, diffuse state to a punctate, aggregated state in “acceptor” cells. To confirm that $mHtt_{ex1}$ nucleates the aggregation of $wtHtt_{ex1}$ in fly neurons, we co-expressed FP-fusions of these two proteins using pan-neuronal *elav[C155]-Gal4*. In flies expressing only mCherry-tagged $mHtt_{ex1}$ (Htt_{ex1}Q91-mCherry) pan-neuronally, aggregates were visible as discrete mCherry+ puncta throughout neuronal cell bodies and neuropil regions of adult fly brains (Fig. 1-figure supplement 1A). By contrast, GFP-tagged $wtHtt_{ex1}$ (Htt_{ex1}Q25-GFP) was expressed diffusely throughout neuronal cell bodies and processes in age-matched adults brains (Fig. 1-figure supplement 1B). Co-expression of these two Htt proteins converted Htt_{ex1}Q25-GFP to a punctate expression pattern that overlapped with Htt_{ex1}Q91-mCherry signal (Fig. 1-figure supplement 1C), whereas the solubility of GFP lacking a polyQ sequence was not affected by Htt_{ex1}Q91-mCherry co-expression (Fig. 1-figure supplement 1D). Thus, prion-like conversion of Htt_{ex1}Q25-GFP occurs only in the presence of Htt_{ex1}Q91-mCherry aggregates and results from a homotypic nucleation reaction rather than $mHtt_{ex1}$-induced global changes to proteostasis in the neuronal cytoplasm.

120 To examine trans-synaptic transfer of mHtt_{ex1} aggregates, we coupled QF-driven expression of
121 Htt_{ex1}Q91-mCherry with Gal4-driven expression of Htt_{ex1}Q25-GFP in neuronal cell populations that
122 make well-defined synaptic connections in the adult fly olfactory system (Fig. 1B). Htt_{ex1}Q91-mCherry
123 was expressed using *Or67d-QF* in presynaptic ORNs (hereafter "DA1 ORNs") that project axons from
124 the antenna into the central brain, where they form synaptic connections with dendrites of partner PNs
125 (hereafter "DA1 PNs") in the DA1 glomerulus of the antennal lobe (Jefferis et al., 2001). In these same
126 animals, Htt_{ex1}Q25-GFP was expressed in ~60% of PNs using *GH146-Gal4*, which labels lateral and
127 ventral DA1 PNs in addition to other PN types (Marin et al., 2002). We did not detect expression of
128 Htt_{ex1}Q91-mCherry in DA1 ORNs until ~24 hr before eclosion, consistent with activation of adult
129 olfactory receptor gene expression during late pupal development (Clyne et al., 1999), whereas
130 Htt_{ex1}Q25-GFP was expressed in PNs much earlier in development (Stocker et al., 1997). Thus, this
131 genetic approach enables us to monitor prion-like transfer of Htt_{ex1}Q91-mCherry aggregates between
132 post-mitotic, synaptically-connected DA1 ORNs and PNs in the adult fly brain.
133 Prion-like transfer of Htt_{ex1}Q91-mCherry aggregates across DA1 ORN-PN synapses was
134 examined by monitoring the solubility of Htt_{ex1}Q91-mCherry and Htt_{ex1}Q25-GFP in or near the DA1
135 glomerulus as the flies aged (Fig. 1B, inset). Puncta representing Htt_{ex1}Q91-mCherry aggregates were
136 detected in the DA1 glomerulus of 1 day-old adults and increased in number over time (Fig. 1C and D).
137 Numbers of Htt_{ex1}Q91-mCherry aggregates in males exceeded those in females at each time point
138 tested, consistent with known sexual dimorphism in DA1 glomerular volume (Stockinger et al., 2005). In
139 these same brains, Htt_{ex1}Q25-GFP was expressed diffusely in GH146+ PN cell bodies and dendrites in
140 1 day-old adults, but induced Htt_{ex1}Q25-GFP aggregates appeared in low quantities in the DA1
141 glomerulus of young adults and accumulated as the flies aged (Fig. 1C and E). Though rare, Htt_{ex1}Q25-
142 GFP aggregates also appeared in PN soma in older adults (Fig. 1F and G), suggesting that these
143 aggregates have the capacity to propagate beyond the DA1 glomerulus. In control experiments,
144 Htt_{ex1}Q25-mCherry in DA1 ORNs did not alter Htt_{ex1}Q25-GFP solubility in PNs (Fig. 1-figure supplement
145 2A,E,F), and the solubility of GFP expressed in PNs was unaffected by Htt_{ex1}Q91-mCherry expression
146 in DA1 ORNs (Fig. 1-figure supplement 2B,E,F). In addition, seeded Htt_{ex1}Q25-GFP aggregates still

147 appeared when the Gal4 inhibitor Gal80 was expressed in ORNs (Fig. 1-figure supplement 2C,E,F) or
148 when the QF repressor QS was expressed in PNs (Fig. 1-figure supplement 2D,E,F), arguing strongly
149 against the possibility that Htt_{ex1}Q91-mCherry and Htt_{ex1}Q25-GFP were co-expressed in any cells in
150 these transgenic animals. Because Htt_{ex1}Q25-GFP did not aggregate in the absence of Htt_{ex1}Q91-
151 mCherry expression (Fig. 1-figure supplement 1B), these findings indicate that the solubility of
152 Htt_{ex1}Q25-GFP in postsynaptic PNs was non-cell autonomously altered by Htt_{ex1}Q91-mCherry
153 aggregates formed in presynaptic ORNs.

154 Importantly, Htt_{ex1}Q25-GFP aggregates were not detected in any other glomeruli labeled by
155 *GH146-Gal4* in these flies (Fig. 1C), suggesting that prion-like conversion of Htt_{ex1}Q25-GFP in PNs by
156 Htt_{ex1}Q91-mCherry aggregates in ORNs requires synaptic connectivity. To examine whether spreading
157 of Htt_{ex1}Q91-mCherry can also occur retrogradely across ORN-PN synapses, we expressed Htt_{ex1}Q91-
158 mCherry in GH146+ PNs and Htt_{ex1}Q25-GFP in all ORNs using *pebbled-Gal4*. While many Htt_{ex1}Q91-
159 mCherry aggregates were formed in PN soma, dendrites, and axons, we saw no evidence of seeded
160 Htt_{ex1}Q25-GFP aggregation in ORN axons in the antennal lobe (Fig. 1-figure supplement 3), indicating
161 that Htt_{ex1}Q91-mCherry spreading across ORN-PN synapses is restricted to or much more efficient in
162 the anterograde direction. Interestingly, we found that aggregates formed by $mHtt_{ex1-12}$ caspase-6
163 cleavage products (RFP-Htt_{ex1-12}Q138) (Fig. 1A) (Graham et al., 2006), which have previously been
164 shown to spread from ORN axons to more distant (non-PN) neurons in the fly CNS (Babcock and
165 Ganetzky, 2015), also transfer across DA1 ORN-PN synapses in our model (Fig. 1H). Thus, the ability
166 to spread trans-synaptically is shared by multiple pathogenic N-terminal mHtt fragments, and the
167 sequences required for prion-like conversion of wtHtt reside within Htt_{ex1}.

168

169 *$wtHtt_{ex1}$ aggregates in PNs are seeded by smaller $mHtt_{ex1}$ aggregates originating in ORNs*

170 Further examination of confocal stacks of the DA1 glomerulus from flies expressing Htt_{ex1}Q91-
171 mCherry in DA1 ORNs and Htt_{ex1}Q25-GFP in GH146+ PNs (Fig. 2A-D) indicated that the vast majority
172 (>95%) of induced Htt_{ex1}Q25-GFP aggregates co-localized with Htt_{ex1}Q91-mCherry puncta (arrows in
173 Fig. 2B and D). This suggests that the solubility of Htt_{ex1}Q25-GFP in PNs was altered upon direct

174 physical interaction with Htt_{ex1}Q91-mCherry seeds from DA1 ORNs. In support of this, fluorescence
175 resonance energy transfer (FRET) analysis showed that the FP tags on Htt_{ex1}Q91-mCherry and
176 Htt_{ex1}Q25-GFP were within ~100Å in all co-localized aggregates tested (Fig. 2E). While nearly all
177 Htt_{ex1}Q25-GFP aggregates in the DA1 glomerulus co-localized with Htt_{ex1}Q91-mCherry seeds, this was
178 true of only a small proportion of Htt_{ex1}Q25-GFP aggregates in PN soma (Fig. 1F and G), suggesting
179 that aggregate fragmentation may drive propagation outside of the antennal lobe neuropil. Interestingly,
180 volumetric analysis of all mCherry+ aggregates in the DA1 glomerulus revealed that seeding-competent
181 Htt_{ex1}Q91-mCherry aggregates belonged to a smaller-sized subpopulation (range = 0.1–2.2 μm^3; mean
182 = 0.859 $\pm$ 0.052 μm^3), whereas the entire population of Htt_{ex1}Q91-mCherry aggregates was more
183 heterogeneously-sized (range = 0.1–9 μm^3; mean = 2.676 $\pm$ 0.046 μm^3) (Fig. 2F). We previously
184 reported that Htt_{ex1}Q25-YFP aggregates formed in the glial cytoplasm co-localized with a similarly
185 smaller-sized subpopulation of Htt_{ex1}Q91-mCherry aggregates from DA1 ORN axons (Pearce et al.,
186 2015), and smaller $mHtt_{ex1}$ aggregates are associated with increased seeding-propensity and
187 neurotoxicity in other HD models (Ast et al., 2018; Chen et al., 2001). Taken together, these findings
188 strongly suggest that Htt_{ex1}Q91-mCherry aggregates formed in presynaptic ORNs gain access to the
189 cytoplasm of postsynaptic PNs to effect prion-like conversion of Htt_{ex1}Q25-GFP, and that Htt_{ex1}Q91-
190 mCherry aggregate transmissibility is inversely correlated with aggregate size.
191
192 *$mHtt_{ex1}$ aggregate transfer is enhanced across silenced DA1 ORN-PN synapses*
193 Endocytosis, exocytosis, and neuronal activity have been previously implicated in neuron-to-
194 neuron spreading of mHtt and other pathogenic aggregates (Babcock and Ganetzky, 2015; Pecho-
195 Vrieseling et al., 2014; Wu et al., 2016), but it is not known how these processes could contribute to
196 aggregate transfer across endogenous synapses *in vivo*. To examine a role for synaptic activity in DA1
197 ORN-to-PN transfer of $mHtt_{ex1}$ aggregates, we used well-established genetic tools that block fission or
198 fusion of synaptic vesicles at the presynaptic membrane, thereby impairing neurotransmission. First, we
199 used *shibire^{ts1}* (*shi^{ts1}*) (Kosaka and Ikeda, 1983), a temperature-sensitive mutant of the GTPase
200 Shibire/dynamin that blocks endocytic recycling of synaptic vesicles in flies raised at the restrictive

201 temperature. Co-expression of shi^{ts1} with Htt$_{ex1}$Q91-mCherry in DA1 ORNs in adult flies raised at 31°C
202 did not affect numbers of Htt$_{ex1}$Q91-mCherry aggregates in the DA1 glomerulus (Fig. 3A and B), but,
203 surprisingly, strongly enhanced formation of Htt$_{ex1}$Q25-GFP aggregates in DA1 PN dendrites (Fig. 3A
204 and C) compared to control flies expressing LacZ. Likewise, co-expression of Htt$_{ex1}$Q91-mCherry with
205 tetanus toxin light chain (TeTxLC), which inhibits SNARE-mediated fusion of synaptic vesicles with
206 presynaptic membranes (Sweeney et al., 1995), had no consistent effect on Htt$_{ex1}$Q91-mCherry
207 aggregate numbers in ORN axons (Fig. 3D and E), but strongly increased numbers of Htt$_{ex1}$Q25-GFP
208 aggregates in the DA1 glomerulus (Fig. 3D and F). To manipulate neuronal activity by an alternative
209 approach, we co-expressed the heat-activated *Drosophila* transient-receptor potential A (dTrpA)
210 channel (Hamada et al., 2008) with Htt$_{ex1}$Q91-mCherry to thermogenetically stimulate DA1 ORNs. In
211 adult flies shifted from 25°C to 31°C upon eclosion, dTrpA-mediated activation of Htt$_{ex1}$Q91-mCherry-
212 expressing DA1 ORNs slightly increased Htt$_{ex1}$Q91-mCherry aggregate numbers (Fig. 3G and H), but
213 substantially decreased formation of Htt$_{ex1}$Q25-GFP aggregates in the DA1 glomerulus (Fig. 3G and I)
214 compared to control flies expressing LacZ. Together, these results suggest that the ability of
215 presynaptic ORNs to fire is inversely correlated with prion-like transfer of Htt$_{ex1}$Q91-mCherry
216 aggregates from ORNs to PNs, perhaps reflecting enhanced aggregate transfer across dysfunctional
217 synapses characteristic of HD and other neurodegenerative diseases.
218 Our results using shi^{ts1} and TeTxLC to block DA1 ORN activity contrast with previous reports
219 showing that spreading of RFP-Htt$_{ex1-12}$Q138 aggregates from ORN axons to non-synaptically
220 connected neurons was slowed when endocytosis or exocytosis was impaired in ORNs (Babcock and
221 Ganetzky, 2015) or that botulinum toxin inhibited spreading of mHtt$_{ex1}$ from R6/2 mouse brain slices to
222 functionally-connected human neurons (Pecho-Vrieseling et al., 2014). We therefore wondered whether
223 blocking Shibire-mediated endocytosis in ORNs might create a more favorable environment for
224 aggregate transfer across endogenous synapses in our HD model. To test this, we first quantified
225 Htt$_{ex1}$Q91-mCherry-expressing DA1 ORN axonal surfaces using membrane-targeted GFP (mCD8-GFP)
226 (Fig. 4A), a tool widely used to label neuronal membranes (Lee and Luo, 1999; Mosca and Luo, 2014)
227 and quantify neuron abundance (Burr et al., 2014; MacDonald et al., 2006) in fly brains. Three-

228 dimensional image analysis (Fig. 4B) revealed that the intensity and volume occupied by ORN axonal
229 membranes in the DA1 glomerulus were increased ~2-fold in shi^{ts1}-expressing flies raised at 31°C as
230 compared to controls (Fig. 4A-C). Because numbers of Htt_{ex1}Q91-mCherry aggregates were unaffected
231 by shi^{ts} expression in DA1 ORNs (Fig. 3B), this finding suggests that blocking endocytosis increases
232 the surface area of DA1 ORN axons, perhaps reflecting a homeostatic compensatory mechanism
233 (Davis, 2013) that could create additional exit sites for Htt_{ex1}Q91-mCherry aggregates.
234 We have previously reported that phagocytic glia engulf Htt_{ex1}Q91-mCherry aggregates from
235 DA1 ORNs, resulting in prion-like conversion of Htt_{ex1}Q25-YFP aggregates in the glial cytoplasm
236 (Pearce et al., 2015). To test whether blocking Shibire-mediated endocytosis in ORNs could also
237 enhance ORN-to-glia transfer of Htt_{ex1}Q91-mCherry aggregates, we co-expressed shi^{ts1} with Htt_{ex1}Q91-
238 mCherry in DA1 ORNs and monitored formation of Htt_{ex1}Q25-YFP aggregates in the glial cytoplasm.
239 Similar to effects of shi^{ts1} on trans-synaptic Htt_{ex1}Q91-mCherry aggregate transfer, blocking Shibire-
240 mediate endocytosis in DA1 ORNs increased Htt_{ex1}Q25-YFP aggregate formation in glia without
241 affecting Htt_{ex1}Q91-mCherry aggregate numbers (Fig. 4D, E, and F). These findings suggest that
242 blocking endocytosis in Htt_{ex1}Q91-mCherry-expressing ORNs alters axonal membrane turnover and
243 stimulates prion-like transfer of Htt_{ex1}Q91-mCherry aggregates from ORNs to both PNs and phagocytic
244 glia, the latter of which we previously showed is mediated by Draper-dependent glial phagocytosis
245 (Pearce et al., 2015).
246
247 *Glial Draper mediates ORN-to-PN transfer and alters morphology of neuronal $mHtt_{ex1}$ aggregates*
248 The parallel effects of shi^{ts1}-mediated endocytic inhibition on transfer of Htt_{ex1}Q91-mCherry
249 aggregates from DA1 ORNs to DA1 PNs and to glia suggest that $mHtt_{ex1}$ aggregate spreading between
250 these cell types is coordinated. We previously reported that ORN-to-glia transfer of Htt_{ex1}Q91-mCherry
251 aggregates is strictly dependent on Draper (Pearce et al., 2015), a scavenger receptor responsible for
252 phagocytic engulfment and clearance of neuronal debris in the fly CNS and other tissues (Etchegaray
253 et al.; Han et al., 2014; Hoopfer et al., 2006; MacDonald et al., 2006). Therefore, we sought to
254 determine whether Draper-dependent phagocytic glia might play a role in transferring $mHtt_{ex1}$

255 aggregates from ORNs to PNs. To test this, we quantified numbers of Htt_{ex1}Q91-mCherry and
256 Htt_{ex1}Q25-GFP aggregates in DA1 ORN axons and PN dendrites, respectively, in animals heterozygous
257 or homozygous for the *draper(drpr)*$^{\Delta 5}$ null mutation (Freeman et al., 2003). As we have previously
258 reported (Pearce et al., 2015), *drpr* knockout increased steady-state numbers of Htt_{ex1}Q91-mCherry
259 aggregates in DA1 ORN axons (Fig. 5A and B), but strikingly, abolished formation of Htt_{ex1}Q25-GFP
260 aggregates in PNs (Fig. 5A and C). *Drpr* knockout also completely blocked formation of Htt_{ex1}Q25-GFP
261 aggregates in PNs when shi^{ts1} was co-expressed with Htt_{ex1}Q91-mCherry in ORNs (Fig. 5-figure
262 supplement 1), confirming that enhanced transfer of Htt_{ex1}Q91-mCherry aggregates from shi^{ts1}-
263 expressing ORNs occurs via the same Draper-dependent mechanism. To rule out the possibility that
264 *GH146-Gal4* drives expression of Htt_{ex1}Q25-GFP in some Draper+ glia, we showed that repo-Gal80-
265 mediated inhibition of Gal4 in all glia had no effect on Htt_{ex1}Q91-mCherry or Htt_{ex1}Q25-GFP aggregate
266 numbers (Fig. 5-figure supplement 2A, C, and D). Moreover, expression of *drpr*-specific siRNAs in PNs
267 had no effect on Htt_{ex1}Q25-GFP aggregate formation, consistent with glia being the sole source of *drpr*
268 expression in the CNS (Fig. 5-figure supplement 2B, C, and D). We also did not observe co-localization
269 between ORN-derived Htt_{ex1}Q91-mCherry aggregates and GFP-tagged versions of Lamp1
270 (Pulipparacharuvil et al., 2005) or Atg8a (Juhász et al., 2008) in glia (Fig. 5-figure supplement 3),
271 suggesting that neuronal Htt_{ex1}Q91-mCherry aggregates do not seed Htt_{ex1}Q25-GFP in glial lysosomes
272 or autophagosomes.

273 These results point to a central role for glial Draper in Htt_{ex1}Q91-mCherry aggregate transfer
274 between multiple cell types in the fly CNS, but how phagocytic glia could mediate spreading of
275 Htt_{ex1}Q91-mCherry aggregates across neuronal synapses was not clear. Intriguingly, the average
276 volume of Htt_{ex1}Q91-mCherry aggregates in the DA1 glomerulus significantly increased from 2.201 ±
277 0.044 μm^3 in wild-type animals to 2.431 ± 0.038 μm^3 in *drpr*-knockout animals ($p < 0.0001$ by Student's
278 *t*-test), and the relative frequency of two aggregate subpopulations shifted between these groups: in the
279 absence of *drpr*, the proportion of a smaller-sized subpopulation ("A", ~0.1-0.5 μm^3) decreased while a
280 larger-sized subpopulation ("B", ~2.5-4.0 μm^3) increased in abundance (Fig. 5D). The decreased
281 frequency of subpopulation A aggregates in $drpr^{\Delta 5/\Delta 5}$ flies was especially interesting because these

282 aggregates closely correlate in volume with those of seeding-competent Htt_{ex1}Q91-mCherry aggregates
283 in PNs (Fig. 2F) or in glia (Pearce et al., 2015). Thus, these results suggest that phagocytic glia
284 mediate transfer of Htt_{ex1}Q91-mCherry aggregates across neuronal synapses, at least in part by
285 promoting the formation of a subpopulation of smaller, transmission-competent neuronal $mHtt_{ex1}$
286 aggregates.
287
288 *Caspase activation in ORNs regulates trans-synaptic transfer of $mHtt_{ex1}$ aggregates*
289 Phagocytic glia engulf injured or degenerating neuronal processes and apoptotic cell corpses by
290 recognizing "eat me" signals exposed on these debris (Wilton et al., 2019). Thus, we asked whether
291 Htt_{ex1}Q91-mCherry aggregate-expressing DA1 ORNs might expose cell surface signals that could drive
292 Draper-dependent transfer of aggregates to DA1 PNs. mHtt expression induces caspase-dependent
293 cell death pathways in fly and mammalian models of HD (Ahmed et al., 2014), and we observed that in
294 *drpr*-deficient flies, *Drosophila* caspase-1 (Dcp-1) immunoreactivity was increased in ORN axons
295 expressing Htt_{ex1}Q91-GFP as compared to controls expressing Htt_{ex1}Q25-GFP (Fig. 6A and B). In
296 addition, co-expression of the viral effector caspase inhibitor p35 (Hay et al., 1994) with Htt_{ex1}Q91-
297 mCherry in DA1 ORNs inhibited formation of Htt_{ex1}Q25-GFP aggregates in DA1 PNs (Fig. 6C and E,
298 *squares*), indicating that caspase activation in presynaptic ORNs is required for $mHtt_{ex1}$ aggregate
299 transfer to postsynaptic PNs. Caspase inhibition also increased numbers of Htt_{ex1}Q91-mCherry
300 aggregates in the DA1 glomerulus (Fig. 6C and D, *squares*), phenocopying effects seen in $drpr^{\Delta 5/\Delta 5}$
301 brains (Fig. 5A and B). Conversely, co-expression of p35 with Htt_{ex1}Q25-GFP in PNs did not affect
302 numbers of Htt_{ex1}Q91-mCherry and Htt_{ex1}Q25-GFP aggregates in the DA1 glomerulus (Fig. 6D and E,
303 *circles*), indicating that caspase-dependent signaling in PNs does not regulate $mHtt_{ex1}$ aggregate
304 spreading across ORN-PN synapses. Together, these results suggest that Htt_{ex1}Q91-mCherry-induced
305 caspase activation in ORN axons signals for engulfment and trans-synaptic transfer of Htt_{ex1}Q91-
306 mCherry aggregates via Draper-dependent phagocytic glia.
307
308 *$mHtt_{ex1}$ aggregates transfer from ORNs to PNs via the glial cytoplasm*

309 The strict requirement for Draper in prion-like transfer of Htt_{ex1}Q91-mCherry aggregates across
310 ORN-PN synapses can be explained by two non-mutually exclusive models. In one model (Fig. 7A,
311 *route 1*), Htt_{ex1}Q91-mCherry aggregates spread from presynaptic ORNs to postsynaptic PNs via a glial
312 cytoplasmic intermediate. This model is consistent with our previous finding that phagocytosed
313 neuronal Htt_{ex1}Q91-mCherry aggregates enter the glial cytoplasm and effect prion-like conversion of
314 Htt_{ex1}Q25-YFP (Pearce et al., 2015). Alternatively (Fig. 7A, *route 2*), Draper-dependent phagocytic glia
315 could sculpt the synaptic environment in a way that promotes transfer of $mHtt_{ex1}$ aggregates directly
316 from ORN axons to PN dendrites. To distinguish between these models, we generated transgenic flies
317 that use three binary expression systems (QF-QUAS, Gal4-UAS, and LexA-LexAop) to independently
318 express a uniquely-tagged Htt_{ex1} transgene in each of three cell populations: Htt_{ex1}Q91-mCherry in DA1
319 ORNs, Htt_{ex1}Q25-3xHA in repo+ glia, and Htt_{ex1}Q25-YFP in GH146+ PNs (Fig. 7A). If Htt_{ex1}Q91-
320 mCherry aggregates formed in presynaptic ORNs travel through the glial cytoplasm to postsynaptic
321 PNs, the same Htt_{ex1}Q91-mCherry aggregate seeds should template the aggregation of Htt_{ex1}Q25-
322 3xHA in glia and Htt_{ex1}Q25-YFP in PNs, resulting in appearance of triple-labeled
323 mCherry+/3xHA+/YFP+ puncta in the DA1 glomerulus (Fig. 7A, *route 1*). A transient subpopulation of
324 double-labeled mCherry+/3xHA+ intermediates might also be observed, but these would be converted
325 to mCherry+/3xHA+/YFP+ aggregates over time. Alternatively, if Htt_{ex1}Q91-mCherry aggregates do not
326 access the glial cytoplasm *en route* to PNs, only double-labeled mCherry+/3xHA+ and mCherry+/YFP+
327 aggregates would appear in the DA1 glomerulus and persist over time (Fig. 7A, *route 2*).
328 Transgenic flies expressing these differentially-tagged Htt_{ex1} transgenes in three distinct CNS
329 cell types were generated, and no overlapping expression of any two transgenes was detected by
330 confocal microscopy (Fig. 7B and C). Htt_{ex1}Q91-mCherry expression was low and largely diffuse in
331 young (0-1 day-old) adult flies, but became more punctate as the flies aged (Fig. 7B-D).
332 mCherry+/3xHA+ puncta representing Htt_{ex1}Q91-mCherry aggregates that had transferred from ORNs
333 to glia began to appear in 2 day-old adults, increased in number during the next 24 hr, but thereafter
334 stabilized as the flies aged (Fig. 7C and E, *white bars*). Strikingly though, small numbers of
335 mCherry+/3xHA+/YFP+ puncta appeared in 2 day-old adults and steadily increased in abundance as

336 the flies aged (Fig. 7C and E, *black bars*), suggesting that these triple-labeled aggregates arose from
337 Htt_{ex1}Q91-mCherry seeds that originated in DA1 ORN axons and transited through the glial cytoplasm
338 before reaching the cytoplasm of DA1 PN dendrites. Notably, mCherry+/YFP+ puncta representing
339 aggregates that directly transferred from DA1 ORNs to DA1 PNs were absent in these brains, arguing
340 against direct transfer of Htt_{ex1}Q91-mCherry aggregates across ORN-PN synapses. Importantly, when
341 *drpr* was depleted specifically in glia by RNAi in these flies, only mCherry+ puncta were visible in the
342 DA1 glomerulus of 7 day-old adults (Fig. 7C, *far right*), confirming that glial Draper mediates aggregate
343 transfer unidirectionally from ORNs to glia to PNs. Taken together, these findings suggest that Draper-
344 dependent glia act as obligatory intermediates in prion-like spreading of $mHtt_{ex1}$ aggregates from
345 presynaptic ORNs to postsynaptic PNs in *Drosophila* brains.
346

347 **DISCUSSION**

348 The hypothesis that prion-like mechanisms underlie the progression of protein aggregate
349 pathology in HD and other neurodegenerative diseases has gained considerable support, but the
350 mechanisms underlying cell-to-cell aggregate transmission *in vivo*, the influences of cell- and region-
351 specific vulnerability, and the relevance of aggregate spreading to disease progression remain unclear.
352 In this study, we report that prion-like transfer of $mHtt_{ex1}$ aggregates from presynaptic ORNs to
353 postsynaptic PNs occurs via Draper-dependent phagocytic glia in transgenic *Drosophila* brains. ORN-
354 to-PN transmission of $mHtt_{ex1}$ aggregates was enhanced by blocking presynaptic endocytosis and
355 exocytosis and slowed by thermogenetically stimulating ORNs, suggesting an inverse relationship
356 between presynaptic neuronal activity and $mHtt_{ex1}$ aggregate transmission across synapses. Endocytic
357 inhibition in ORNs also enhanced ORN-to-glia $mHtt_{ex1}$ transfer in the antennal lobe, suggesting that
358 neuronal silencing stimulates Draper-dependent phagocytosis of aggregate-containing ORN axons and
359 presumably subsequent transfer to postsynaptic PNs. We also find that trans-synaptic $mHtt_{ex1}$
360 aggregate transfer requires caspase activity in ORNs and is completely blocked in *drpr*-knockout
361 animals, suggesting that Draper-dependent glia recognize caspase-dependent "eat me" signals (e.g.
362 exposed phosphatidylserine) on the surface of $mHtt_{ex1}$-expressing axons to initiate phagocytic
363 engulfment. Remarkably, a portion of $mHtt_{ex1}$ aggregates originating in ORN axons effect prion-like
364 conversion of cytoplasmic $wtHtt_{ex1}$ proteins first in glia and then in PN dendrites, indicating that
365 aggregates transfer from presynaptic ORNs to postsynaptic PNs through a Draper-dependent glial
366 cytoplasmic intermediate. These findings expand our understanding of the beneficial and harmful
367 effects of phagocytic glia in neurodegeneration—while phagocytic engulfment and lysosomal
368 degradation clear neurotoxic aggregates and cell corpses from the brain, escape of even a few
369 engulfed aggregates from the phagolysosomal system generates a glial cytoplasmic reservoir of prion-
370 like aggregate species that can propagate further in the CNS.

371 Though HD is a monogenic disorder and the Htt gene is expressed ubiquitously, it is plausible
372 that prion-like spreading of mHtt aggregates could drive progression of HD pathology from more
373 vulnerable regions of the brain to those less susceptible to mHtt aggregation. We find that $mHtt_{ex1}$

374 aggregate transmission across ORN-PN synapses occurs selectively in the anterograde direction and
375 is inversely correlated with synaptic activity, suggesting that aggregate spreading is enhanced across
376 dysfunctional synapses, an early molecular feature of HD and other neurodegenerative diseases.
377 Intriguingly, the earliest pathological changes in HD patient brains involve loss of cortical inputs to the
378 striatum, where more prominent pathological findings (i.e., mHtt aggregate accumulation and massive
379 loss of medium spiny neurons) appear in later stages of disease (Reiner and Deng, 2018). Moreover,
380 selective silencing of mHtt expression in both the cortex and striatum produced the most beneficial
381 effects on striatal degeneration and motor phenotypes in BACHD mice (Wang et al., 2014), suggesting
382 that mHtt-induced toxicity in presynaptic cortical regions may play a major role in early HD
383 neuropathogenesis. Our results demonstrating increased aggregate transfer from activity-impaired
384 ORN axons conflict with reports from other groups showing that neuronal silencing slows cell-to-cell
385 spreading of mHtt in fly brains (Babcock and Ganetzky, 2015) or mixed-species *ex vivo* co-cultures
386 (Pecho-Vrieseling et al., 2014). This discrepancy could be due to construct- or cell type-specific effects,
387 or could possibly reflect different mechanisms regulating synaptic or non-synaptic aggregate
388 transmission in the brain. Our HD model differs from these others in that we monitored mHtt aggregate
389 spreading across endogenous synapses formed under physiological conditions. Thus, our findings
390 uncovering unexpected roles for presynaptic silencing and phagocytic glia in aggregate transfer likely
391 reflect intimate relationships that glia make with neuronal synapses in intact brains.
392 Central roles for phagocytic glia in neurodegeneration are becoming increasingly recognized as
393 genome-wide association studies and transcriptomic analyses identify glial genes associated with
394 increased risk or development of disease. For example, rare variants in *TREM2*, a gene that encodes a
395 microglial phagocytic receptor, are associated with increased risk of AD, FTD, and PD, and loss of
396 TREM2 function exacerbates Aβ-, tau-, and α-synuclein-associated neurotoxicity (Griciuc et al.; Guo et
397 al., 2019; Leyns et al., 2019; Zhao et al., 2018). Reactive glia alter their morphology and gene
398 expression profiles in response to diverse types of injury to promote neuronal survival by releasing
399 trophic factors and clearing debris (Hammond et al., 2018). Phagocytic glia likely play some beneficial
400 roles in neurodegeneration, since pathogenic aggregates accumulate when glial phagocytosis is

401 disrupted (Asai et al., 2015; Hong et al., 2016; Pearce et al., 2015; Ray et al., 2017; Wilton et al., 2019),
402 and administration of antibodies targeting pathological Aβ, tau, and α-synuclein proteins reduces
403 aggregate accumulation and spreading in mouse brains (Funk et al., 2015; Masliah et al., 2005; Tran et
404 al., 2014; Yanamandra et al., 2013). However, chronically active and/or dysfunctional glia constitutively
405 release neuroinflammatory signals and acquire behaviors that exacerbate neuronal damage. For
406 example, hyperactivate microglia excessively phagocytose synapses in pre-plaque AD mouse brains
407 (Hong et al., 2016) and induce the formation of neurotoxic A1 astrocytes that persist in many
408 neurodegenerative diseases (Liddelow et al., 2017; Yun et al., 2018) and during aging (Clarke et al.,
409 2018). Our findings thus add new insights to recognizing glia as double-edged players in
410 neurodegeneration and suggest that rebalancing the protective and harmful effects of phagocytic glia
411 could be a promising new therapeutic strategy.

412 Our data support a model in which Draper-dependent phagocytic glia engulf $mHtt_{ex1}$ aggregates
413 or portions of $mHtt_{ex1}$-expressing ORN axons exposing caspase-dependent signals to promote neuron
414 survival; however, this same process leads to prion-like aggregate spreading to glial and PN
415 cytoplasms. We provide several lines of evidence to support our conclusion that phagocytosed $mHtt_{ex1}$
416 aggregates access the cytoplasm of glia and then PNs and to argue against seeding of $wtHtt_{ex1}$ in the
417 interstitial space. The strict requirement for Draper in ORN-to-glia and ORN-to-glia-to-PN aggregate
418 transfer indicates that neuronal $mHtt_{ex1}$ and glial $wtHtt_{ex1}$ proteins physically interact during or following
419 phagocytic engulfment, requiring breaching of one or more membrane barriers that normally exclude
420 phagocytosed material from the glial cytoplasm. In support of this, prion-like aggregates formed by α-
421 synuclein, tau, and $mHtt_{ex1}$ have the capacity to rupture cell surface or endolysosomal membranes to
422 directly access the cytoplasmic compartment (Chen et al., 2019; Falcon et al., 2018; Flavin et al., 2017;
423 Zeineddine et al., 2015). It is also possible that phagocytosis becomes dysregulated in diseased or
424 aged brains. Indeed, extracellular Aβ or α-synuclein fibrils accumulate inside phagocytic microglia over
425 time (Chung et al., 1999; Frackowiak et al., 1992), and the ability of microglia to degrade phagocytosed
426 material declines with age (Bliederhaeuser et al., 2016; Tremblay et al., 2012). Defects in lysosomal
427 clearance could also mediate aggregate escape, supported by a recent finding that proteins unable to

428 be efficiently digested by autophagolysosomes are excreted by cells in a model of the polyQ disease
429 dentatorubral-pallidoluysian atrophy (Baron et al., 2017). Thus, impairments in phagosome maturation
430 or degradation of engulfed material by the lysosome could increase opportunities for aggregate escape
431 and cell-to-cell spreading.

432 Interestingly, we found that Draper knockout is associated with loss of smaller-sized, seeding-
433 competent $mHtt_{ex1}$ aggregates in ORN axons, suggesting that the Draper phagocytic pathway regulates
434 neuronal $mHtt_{ex1}$ aggregate size. How phagocytic glia could alter the morphology of neuronal $mHtt_{ex1}$
435 aggregates is not immediately clear, but it is possible that dynamin-mediated fission or SNARE-
436 mediated fusion events during phagosome maturation could generate aggregate fragments that fall
437 below an upper size limit for entry to the cytoplasm and/or can directly penetrate intracellular
438 membranes. Draper could also selectively deplete a subpopulation of larger neuronal aggregates from
439 which smaller transmissible species are produced. Interestingly, seeding propensity is correlated with
440 smaller $mHtt_{ex1}$ aggregate size in other HD models (Ast et al., 2018; Chen et al., 2001), and secondary
441 nucleation processes initiated by aggregate fragmentation are thought to drive amplification of prion-like
442 particles in many neurodegenerative diseases (Knowles et al., 2014).

443 One of the most striking results we report here is that all induced $wtHtt_{ex1}$ aggregates in PNs
444 arise from ORN-derived $mHtt_{ex1}$ aggregates that escaped from Draper-dependent phagocytosis into the
445 glial cytoplasm. How could phagocytosed $mHtt_{ex1}$ aggregates transfer from the glial cytoplasm to the
446 cytoplasm of postsynaptic PNs? Several mechanisms already proposed for prion-like aggregate
447 spreading could support inter-cytoplasmic transfer between these cells, including transport through
448 membrane-protected compartments such as extracellular vesicles or tunneling nanotubes, secretion or
449 passive release of aggregates from dying cells, and/or direct penetration of lipid bilayers (Brundin et al.,
450 2010; Davis et al., 2018; Vaquer-Alicea and Diamond, 2019). However, none of these mechanisms
451 discriminate between transfer of aggregates directly from ORNs to PNs or from glia to PNs, suggesting
452 that escape of aggregates from phagocytic glia must involve a mechanism that is unique to these cells
453 in the disease state. In support of this, pathological tau transfers between cultured cells or anatomically-
454 connected regions of mouse brains via exosomes secreted by microglia (Asai et al., 2015), suggesting

455 that phagocytic glia could facilitate prion-like spreading via exosomal release after engulfed neuronal
456 aggregates have reached the glial cytoplasm. Further studies are needed to elucidate the role of
457 phagocytic glia in aggregate propagation and the mechanistic details for intracellular aggregate
458 propagation between diverse cell types in the CNS.

459 Our findings support a mechanism in which glia engulf $mHtt_{ex1}$ aggregates from ORN axons
460 without phagocytosing elements of PNs because (i) $mHtt_{ex1}$ aggregate transmission only occurred in
461 the anterograde direction across ORN-PN synapses, (ii) $wtHtt_{ex1}$ aggregates were observed in PN cell
462 bodies, (iii) $mHtt_{ex1}$ aggregates did not co-localize with markers of lysosomes or autophagosomes in
463 glia, and (iv) caspase inhibition in ORNs and not in PNs slowed aggregate transfer. In developing
464 mouse brains, pruned presynaptic structures are observed within microglia largely in the absence of
465 postsynaptic markers (Schafer et al., 2012; Weinhard et al., 2018), suggesting that glia selectively
466 "nibble" presynaptic components through a process known as trogocytosis. Interestingly, mammalian
467 astrocytes expressing the Draper homolog MEGF10 and complement-dependent microglia
468 preferentially engulf less active, "weaker" synapses to refine neural circuits in developing and adult
469 mouse brains (Chung et al., 2013; Schafer et al., 2012), and aberrant activation of these pathways
470 could contribute to early synaptic loss in neurodegenerative diseases (Hong et al., 2016). Our finding
471 that transfer of $mHtt_{ex1}$ aggregates to glia and PNs was enhanced when ORNs were silenced suggests
472 that phagocytic glia become activated to clear dysfunctional, aggregate-containing presynaptic
473 structures that accumulate early in HD and other in neurodegenerative diseases, ultimately leading to
474 propagation of prion-like aggregate species along synaptic connections in the brain.

475 In summary, our data demonstrate that $mHtt_{ex1}$ aggregates undergo prion-like transfer between
476 synaptically-connected neurons via Draper-dependent glia, raising the intriguing possibility that
477 phagocytic glia could act as a mobile vehicle to spread neuronal aggregate pathology through the CNS.
478 These findings have important implications for understanding complex relationships between
479 aggregate-induced cytotoxicity and communication between neuronal and glial cell types in health and
480 disease. Deciphering the mechanisms that underlie helpful and harmful phagocytic glial cell functions in

481 the degenerating brain will help to reveal new ways in which glia can be targeted therapeutically in

482 neurodegenerative diseases.

483 **MATERIALS AND METHODS**

484 *Fly husbandry*

485 All fly stocks and crosses were raised on standard cornmeal/molasses media at 25°C, ~50%
486 relative humidity, and on a 12 hr light/12 hr dark cycle, unless otherwise noted. The following drivers
487 were used to genetically access different cell populations in the fly CNS: *elav[C155]-Gal4* (Lin and
488 Goodman, 1994), *Or67d-QF* (Liang et al., 2013), *GH146-Gal4* (Stocker et al., 1997), *GH146-QF* (Potter
489 et al., 2010), and *GH146-LexA::GAD* (Lai et al., 2008) (a kind gift from Tzumin Lee, Janelia Farms),
490 *repo-Gal4* (Sepp et al., 2001), and *Or83b-Gal4* (Kreher et al., 2005). Transgenic flies previously
491 described by our lab include *QUAS-Htt$_{ex1}$Q91-mCherry*, *QUAS-Htt$_{ex1}$Q25-mCherry*, *UAS-Htt$_{ex1}$Q91-*
492 *mCherry*, *UAS-Htt$_{ex1}$Q25-GFP*, *UAS-Htt$_{ex1}$Q25-YFP*, and *UAS-GFP* transgenes inserted at the attP3
493 (1st chromosome) and/or attP24 (2nd chromosome) ϕC31 integration sites (Pearce et al., 2015). Other
494 transgenic flies not generated in this study include: *QUAS-nucLacZ* lines #7 and 44 (BDSC #30006 and
495 30007), *QUAS-shi^{ts1}* lines #2, 5, and 7 (BDSC #30010 and 30012; kind gift from C. Potter, Johns
496 Hopkins School of Medicine), *QUAS-TeTxLC* lines #4c and 9c and *QUAS-dTrpA* lines #5, 6, and 7
497 (kind gifts from O. Riabinina and C. Potter, Johns Hopkins), *QUAS-mCD8-GFP* line #5J (BDSC
498 #30002), *QUAS-p35* (a kind gift from H. Steller, Rockefeller University), *UAS-LacZ* (BDSC #8529),
499 *UAS-p35* (BDSC #5072), *QUAS-Gal80* (BDSC #51948), *UAS-QS* (BDSC #30033), *repo-Gal80* (a kind
500 gift from T. Clandinin, Stanford University), *UAS-FFLuc.VALIUM1* (BDSC #35789), *UAS-GFP-Lamp1*
501 (BDSC #42714), *UAS-Atg8a-GFP* (BDSC #52005), and *UAS-Draper^{RNAi}* and *drpr$^{\Delta 5}$* mutant flies (kind
502 gifts from M. Freeman, Vollum Institute). Genotypes for all flies used in this study are listed in Table 1.
503

504 *Cloning and transgenesis*

505 pUASTattB(Htt$_{ex1}$Q25-GFP) and pUASTattB(Htt$_{ex1}$Q25-3xHA) plasmids were generated by PCR
506 amplification of tagged Htt$_{ex1}$ cDNAs from the pcDNA3 vector backbone and cloned into pUASTattB via
507 XhoI and XbaI restriction sites. cDNA for mRFP-Htt$_{ex1-12}$Q138 (a kind gift from T. Littleton, MIT) (Weiss
508 et al., 2012) was subcloned into the pQUASTattB plasmid (Riabinina et al., 2015) using EcoRI and XbaI
509 restriction sites. Htt$_{ex1}$Q25-YFP cDNA was amplified by PCR from the pUASTattB(Htt$_{ex1}$Q25-YFP)

510 plasmid (Pearce et al., 2015) and subcloned into the EcoRI site in pLOT downstream of LexA-
511 responsive LexAop DNA sequences. Plasmids were microinjected into embryos containing the attP3 X
512 chromosome (for UAS-Htt$_{ex1}$Q25-GFP), attP3B or attP8 X chromosome (for QUAS-mRFP-Htt$_{ex1-}$
513 $_{12}$Q138), or attP24 2nd chromosome (for UAS-Htt$_{ex1}$Q25-3xHA or LexAop-Htt$_{ex1}$Q25-YFP) ϕC31
514 integration sites either in-house or at BestGene, Inc (Chino Hills, CA).
515
516 *Drosophila brain dissection, immunostaining, and imaging*
517 Adult fly brains were dissected, fixed, and stained and/or imaged as previously described
518 (Pearce et al., 2015). Briefly, brains were dissected in ice-cold phosphate-buffered saline containing
519 either 0.03% Triton X-100 (PBS/0.03T, when intrinsic fluorescence of expressed FP-fusions was to be
520 imaged) or 0.3% Triton X-100 (PBS/0.3T, when using indirect immunofluorescence to detect protein
521 expression). We typically imaged using intrinsic GFP/YFP/mCherry fluorescence when Htt-FP fusions
522 were bright enough to detect on the confocal to reduce sample preparation time needed prior to
523 imaging. Dissected brains were transferred to microfuge tubes containing PBS/T + 4%
524 paraformaldehyde fixative solution on ice and then fixed in the dark at room temperature (RT) for 5 min
525 (when imaging intrinsic fluorescence) or 20 min (when using immunofluorescence). For direct
526 fluorescence imaging, brains were washed in PBS/0.03T buffer several times before incubation in
527 Slowfade Gold Antifade Mountant (Invitrogen, Carlsbad, CA) for at least 1 hr at 4°C in the dark. For
528 immunostaining, brains were washed several times in PBS/0.3T, and then blocked in PBS/0.3T
529 containing 5% normal goat serum (Lampire Biological Laboratories, Pipersville, PA) for 30min at RT,
530 followed by incubation in primary antibodies diluted in blocking solution and incubation for 24-72 hr at
531 4°C in the dark. Brains were then washed in PBS/0.3T several times at RT and incubated in secondary
532 antibodies diluted in blocking solution for 20-24 hr at 4°C in the dark. Following another set of washes
533 in PBS/0.3T at RT, the brains were incubated in Slowfade mountant for at least 16 hr at 4°C in the dark.
534 Primary antibodies used in this study include rabbit anti-DsRed (1:2000; #632496; Takara Bio
535 USA, Inc., Mountain View, CA), rabbit anti-mCherry (1:500; #PA5-34974; Invitrogen, Carlsbad, CA),
536 chicken anti-GFP (1:500; #GFP-1020; Aves Labs, Tigard, OR), chicken anti-GFP (1:1000; #ab13970;

537 Abcam, Cambridge, UK), rat anti-HA (1:100; clone 3F10; #11867423001; Roche, Basel, Switzerland),
538 rabbit anti-cleaved Dcp-1 (1:100; #9578S; Cell Signaling Technology, Danvers, MA), and mouse anti-
539 Bruchpilot (1:100; clone nc82; Developmental Studies Hybridoma Bank, Iowa City, IA). Secondary
540 antibodies used include FITC-conjugated donkey anti-chicken (1:200; #703-095-155; Jackson Immuno
541 Research Labs, West Grove, PA) and AlexaFluor 488, 568, or 647-conjugated goat anti-chicken, anti-
542 mouse, anti-rabbit, or anti-rat IgGs (1:250 each; Invitrogen, Carlsbad, CA).
543
544 *Confocal microscopy and image analysis and quantification*
545 Brains were bridge-mounted in Slowfade mountant on glass microscopy slides overlayed with
546 #1.5 coverglass (22 x 22 mm), and edges were sealed using clear nail polish. All images were collected
547 on Leica SP8 or Zeiss LSM510 laser-scanning confocal systems equipped with 405 nm, 488 nm, 561
548 nm, and 633 nm lasers and 40X 1.3NA or 63X 1.4NA oil objective lenses. Leica LAS X or Zeiss ZEN
549 software programs were used to establish optimal settings during each microscopy session and to
550 collect optical z-slices of whole-mounted brain samples with Nyquist sampling criteria.
551 Raw confocal data were analyzed in 2D using ImageJ/FIJI software (NIH, Bethesda, MD) or in
552 3D using Imaris image analysis software (Bitplane, Zürich, Switzerland). Most images were collected at
553 optical zoom ≥3 to capture the DA1 glomerulus, and the image bounding box served as a region of
554 interest. In Imaris, individual Htt aggregates were identified using the “Surfaces” algorithm (surface
555 detail set to 0.18 μm and background subtraction at 0.45 μm). “Split touching objects” option was
556 selected, and seed point diameter was set to 0.8 μm. Thresholding was adjusted manually for each
557 image, typically within ~5% among samples in the same experiment, to maximally quantify punctate
558 (i.e., aggregate) objects while minimizing background. While these settings permitted accurate counting
559 of most heterogeneously-sized Htt_{ex1}Q91-mCherry aggregates in the DA1 glomerulus, some larger
560 aggregates were aberrantly double-counted or smaller aggregates in close proximity were
561 inappropriately merged. In these rare cases, individual objects were manually unified or split using the
562 Imaris software prior to recording total aggregate counts for each image. Because Htt_{ex1}Q25-
563 G/YFP/3xHA aggregates present in DA1 PNs or glia were harder to discern from surrounding diffuse

564 $Htt_{ex1}Q25$ signal, these puncta were manually counted by scanning individual z-slices to identify co-
565 localized aggregates. To measure DA1 ORN axon volume in the DA1 glomerulus, mCD8-GFP signal
566 was detected using the "Surfaces" function in Imaris (surface detail = 0.2 μm, and background
567 subtraction = 3 μm). Individual aggregate or surface detail measurements (e.g. volume, intensity) were
568 calculated using Imaris, and the data were exported to Excel (Microsoft Corporation, Redmond, WA) or
569 Prism (GraphPad Software, San Diego, CA) software programs for further analysis.
570
571 *FRET analysis*
572 $Htt_{ex1}Q25$-GFP and $Htt_{ex1}Q91$-mCherry co-localized aggregates were analyzed for FRET using
573 the acceptor photobleaching method as previously described (Pearce et al., 2015). Briefly, 28 individual
574 aggregates were analyzed by photobleaching the mCherry acceptor using a 561nm laser set at 100%
575 intensity and scanning until the mCherry signal was no longer detectable. Donor fluorescence
576 dequenching was measured by exciting GFP using a 488 nm laser set at 1% intensity before and after
577 acceptor photobleaching. mCherry fluorescence was also excited before and after photobleaching with
578 a 561 nm laser set at 1% intensity. Fluorescence emission was collected between 500 and 550 nm for
579 GFP and 610 and 700 nm for mCherry to generate before and after images. FRET efficiencies
580 ($FRET_{eff}$) were calculated after background correction using the equation $(GFP_{after}-GFP_{before})/(GFP_{after}) \times$
581 100 and represented by a pixel-by-pixel $FRET_{eff}$ image generated using the FRETcalc plugin
582 (Stepensky, 2007) in FIJI/ImageJ software.
583
584 *Statistical analyses*
585 All quantified data were organized and analyzed in Excel or Prism 8 software programs.
586 Quantifications in graphical form are shown as mean ± SEM, except for frequency analyses, which are
587 displayed in histograms. Results of all statistical analyses are described in each Figure Legend.
588 Sample size is indicated by *n* either directly on graphical panels of figures or in the figure legend and
589 was selected to yield sufficient statistical power (≥ 5 biological replicates for each condition; each
590 individual brain represents a single biological replicate). Multiple statistical comparisons were

591 performed using the following tests and post-hoc corrections where appropriate: Student's *t*-tests for
592 pairwise comparisons, or one-way or two-way ANOVA followed by Sidak's or Tukey's multiple
593 comparison tests, respectively, for experiments involving ≥3 genotypes. Results of these statistical tests
594 are shown on each graph and described in the Figure Legends.

ACKNOWLEDGMENTS

The authors would like to thank K. Chao, D. Luginbuhl, V. Reed, B. Temsamrit, and M. Warkala for technical assistance, G. Panning for help with analyzing volume measurements, T.R. Clandinin, M.R. Freeman, H. Krämer, T. Lee, J.T. Littleton, C.J. Potter, and O. Riabinina for kindly sharing reagents, and members of the Kopito, Luo, and Pearce labs for many valuable discussions. This work was supported by grants from the NIH (R01-DC005982 to L.L., R01-NS042842 to R.R.K, and R03-AG063295 to M.M.P.P.), the W.W. Smith Charitable Trusts (to M.M.P.P.), the Pittsburgh Foundation (UN2018-98318 to M.M.P.P.), and start-up funds from University of the Sciences (to M.M.P.P.).

AUTHOR CONTRIBUTIONS

K.M.D., O.R.D., W.M.T., and G.E.P. – Investigation, Validation, Visualization, Writing – review & editing. L.L. and R.R.K. – Conceptualization, Resources, Supervision, Writing – review & editing, Funding Acquisition. M.M.P.P. – Conceptualization, Methodology, Investigation, Validation, Formal Analysis, Visualization, Writing – original draft preparation, Writing – review & editing, Resources, Supervision, Project Administration, Funding Acquisition.

DECLARATION OF INTERESTS

The authors declare no competing interests.

615 **REFERENCES**

616 Ahmed, Z., Cooper, J., Murray, T.K., Garn, K., McNaughton, E., Clarke, H., Parhizkar, S., Ward, M.A.,
617 Cavallini, A., Jackson, S.*, et al.* (2014). A novel in vivo model of tau propagation with rapid and
618 progressive neurofibrillary tangle pathology: the pattern of spread is determined by connectivity,
619 not proximity. Acta neuropathologica *127*, 667-683.

620 Asai, H., Ikezu, S., Tsunoda, S., Medalla, M., Luebke, J., Haydar, T., Wolozin, B., Butovsky, O., Kügler,
621 S., and Ikezu, T. (2015). Depletion of microglia and inhibition of exosome synthesis halt tau
622 propagation. Nature neuroscience *18*, 1584.

623 Ast, A., Buntru, A., Schindler, F., Hasenkopf, R., Schulz, A., Brusendorf, L., Klockmeier, K., Grelle, G.,
624 McMahon, B., Niederlechner, H.*, et al.* (2018). mHTT Seeding Activity: A Marker of Disease
625 Progression and Neurotoxicity in Models of Huntington's Disease. Molecular cell *71*, 675-
626 688.e676.

627 Babcock, D.T., and Ganetzky, B. (2015). Transcellular spreading of huntingtin aggregates in the
628 Drosophila brain. Proceedings of the National Academy of Sciences of the United States of
629 America *112*, E5427-5433.

630 Baron, O., Boudi, A., Dias, C., Schilling, M., Nolle, A., Vizcay-Barrena, G., Rattray, I., Jungbluth, H.,
631 Scheper, W., Fleck, R.A.*, et al.* (2017). Stall in Canonical Autophagy-Lysosome Pathways
632 Prompts Nucleophagy-Based Nuclear Breakdown in Neurodegeneration. Current biology *27*,
633 3626-3642.e3626.

634 Bates, G.P., Dorsey, R., Gusella, J.F., Hayden, M.R., Kay, C., Leavitt, B.R., Nance, M., Ross, C.A.,
635 Scahill, R.I., Wetzel, R.*, et al.* (2015). Huntington disease. Nature reviews Disease primers *1*,
636 15005.

637 Bliederhaeuser, C., Grozdanov, V., Speidel, A., Zondler, L., Ruf, W.P., Bayer, H., Kiechle, M., Feiler,
638 M.S., Freischmidt, A., Brenner, D.*, et al.* (2016). Age-dependent defects of alpha-synuclein
639 oligomer uptake in microglia and monocytes. Acta neuropathologica *131*, 379-391.

640 Boland, B., Yu, W.H., Corti, O., Mollereau, B., Henriques, A., Bezard, E., Pastores, G.M., Rubinsztein,
641 D.C., Nixon, R.A., Duchen, M.R.*, et al.* (2018). Promoting the clearance of neurotoxic proteins in
642 neurodegenerative disorders of ageing. Nature reviews Drug discovery *17*, 660-688.
643 Braak, H., and Braak, E. (1991). Neuropathological stageing of Alzheimer-related changes. Acta
644 neuropathologica *82*, 239-259.
645 Braak, H., Del Tredici, K., Rub, U., de Vos, R.A., Jansen Steur, E.N., and Braak, E. (2003). Staging of
646 brain pathology related to sporadic Parkinson's disease. Neurobiology of aging *24*, 197-211.
647 Brettschneider, J., Del Tredici, K., Toledo, J.B., Robinson, J.L., Irwin, D.J., Grossman, M., Suh, E., Van
648 Deerlin, V.M., Wood, E.M., Baek, Y.*, et al.* (2013). Stages of pTDP-43 pathology in amyotrophic
649 lateral sclerosis. Annals of neurology *74*, 20-38.
650 Brundin, P., Melki, R., and Kopito, R. (2010). Prion-like transmission of protein aggregates in
651 neurodegenerative diseases. Nature reviews Molecular cell biology *11*, 301-307.
652 Burr, A.A., Tsou, W.-L., Ristic, G., and Todi, S.V. (2014). Using Membrane-Targeted Green Fluorescent
653 Protein To Monitor Neurotoxic Protein-Dependent Degeneration of Drosophila Eyes. Journal of
654 neuroscience research *92*, 1100-1109.
655 Chen, J.J., Nathaniel, D.L., Raghavan, P., Nelson, M., Tian, R., Tse, E., Hong, J.Y., See, S.K., Mok,
656 S.A., Hein, M.Y.*, et al.* (2019). Compromised function of the ESCRT pathway promotes
657 endolysosomal escape of tau seeds and propagation of tau aggregation. The Journal of
658 biological chemistry. Pii: jbc.RA119.009432.
659 Chen, S., Berthelier, V., Yang, W., and Wetzel, R. (2001). Polyglutamine aggregation behavior in vitro
660 supports a recruitment mechanism of cytotoxicity. Journal of molecular biology *311*, 173-182.
661 Chung, H., Brazil, M.I., Soe, T.T., and Maxfield, F.R. (1999). Uptake, degradation, and release of
662 fibrillar and soluble forms of Alzheimer's amyloid beta-peptide by microglial cells. The Journal of
663 biological chemistry *274*, 32301-32308.
664 Chung, W.-S., Clarke, L.E., Wang, G.X., Stafford, B.K., Sher, A., Chakraborty, C., Joung, J., Foo, L.C.,
665 Thompson, A., Chen, C.*, et al.* (2013). Astrocytes mediate synapse elimination through
666 MEGF10 and MERTK pathways. Nature *504*, 394-400.

667 Clarke, L.E., Liddelow, S.A., Chakraborty, C., Munch, A.E., Heiman, M., and Barres, B.A. (2018).
668 Normal aging induces A1-like astrocyte reactivity. Proceedings of the National Academy of
669 Sciences of the United States of America *115*, E1896-e1905.
670 Clyne, P.J., Warr, C.G., Freeman, M.R., Lessing, D., Kim, J., and Carlson, J.R. (1999). A novel family
671 of divergent seven-transmembrane proteins: candidate odorant receptors in Drosophila. Neuron
672 *22*, 327-338.
673 Costanzo, M., Abounit, S., Marzo, L., Danckaert, A., Chamoun, Z., Roux, P., and Zurzolo, C. (2013).
674 Transfer of polyglutamine aggregates in neuronal cells occurs in tunneling nanotubes. Journal
675 of cell science *126*, 3678-3685.
676 Davis, G.W. (2013) Homeostatic signaling and the stabilization of neural function. Neuron *80*, 718-728.
677 Davis, A.A., Leyns, C.E.G., and Holtzman, D.M. (2018). Intercellular Spread of Protein Aggregates in
678 Neurodegenerative Disease. Annual review of cell and developmental biology *34*, 545-568.
679 Deng, Y.P., Albin, R.L., Penney, J.B., Young, A.B., Anderson, K.D., and Reiner, A. (2004). Differential
680 loss of striatal projection systems in Huntington's disease: a quantitative immunohistochemical
681 study. Journal of chemical neuroanatomy *27*, 143-164.
682 Donnelly, K.M., and Pearce, M.M.P. (2018). Monitoring Cell-to-cell Transmission of Prion-like Protein
683 Aggregates in Drosophila Melanogaster. Journal of visualized experiments *12*, 133.
684 Etchegaray, J.I., Elguero, E.J., Tran, J.A., Sinatra, V., Feany, M.B., and McCall, K. (2016). Defective
685 Phagocytic Corpse Processing Results in Neurodegeneration and Can Be Rescued by TORC1
686 Activation. The Journal of neuroscience : the official journal of the Society for Neuroscience *36*,
687 3170-3183.
688 Falcon, B., Noad, J., McMahon, H., Randow, F., and Goedert, M. (2018). Galectin-8-mediated selective
689 autophagy protects against seeded tau aggregation. The Journal of biological chemistry *293*,
690 2438-2451.
691 Flavin, W.P., Bousset, L., Green, Z.C., Chu, Y., Skarpathiotis, S., Chaney, M.J., Kordower, J.H., Melki,
692 R., and Campbell, E.M. (2017). Endocytic vesicle rupture is a conserved mechanism of cellular
693 invasion by amyloid proteins. Acta neuropathologica *134*, 629-653.

694 Frackowiak, J., Wisniewski, H.M., Wegiel, J., Merz, G.S., Iqbal, K., and Wang, K.C. (1992).
695 Ultrastructure of the microglia that phagocytose amyloid and the microglia that produce beta-
696 amyloid fibrils. Acta neuropathologica *84*, 225-233.
697 Freeman, M.R. (2015). Drosophila Central Nervous System Glia. Cold Spring Harbor perspectives in
698 biology *7*, a020552.
699 Freeman, M.R., Delrow, J., Kim, J., Johnson, E., and Doe, C.Q. (2003). Unwrapping glial biology: Gcm
700 target genes regulating glial development, diversification, and function. Neuron *38*, 567-580.
701 Funk, K.E., Mirbaha, H., Jiang, H., Holtzman, D.M., and Diamond, M.I. (2015). Distinct Therapeutic
702 Mechanisms of Tau Antibodies: Promoting Microglial Clearance Versus Blocking Neuronal
703 Uptake. The Journal of biological chemistry *290*, 21652-21662.
704 Graham, R.K., Deng, Y., Slow, E.J., Haigh, B., Bissada, N., Lu, G., Pearson, J., Shehadeh, J., Bertram,
705 L., Murphy, Z.*, et al.* (2006). Cleavage at the caspase-6 site is required for neuronal dysfunction
706 and degeneration due to mutant huntingtin. Cell *125*, 1179-1191.
707 Grathwohl, S.A., Kalin, R.E., Bolmont, T., Prokop, S., Winkelmann, G., Kaeser, S.A., Odenthal, J.,
708 Radde, R., Eldh, T., Gandy, S.*, et al.* (2009). Formation and maintenance of Alzheimer's
709 disease beta-amyloid plaques in the absence of microglia. Nature neuroscience *12*, 1361-1363.
710 Griciuc, A., Patel, S., Federico, A.N., Choi, S.H., Innes, B.J., Oram, M.K., Cereghetti, G., McGinty, D.,
711 Anselmo, A., Sadreyev, R.I.*, et al.* (2019). TREM2 Acts Downstream of CD33 in Modulating
712 Microglial Pathology in Alzheimer's Disease. Neuron *103*, 820-835.e827.
713 Guo, Y., Wei, X., Yan, H., Qin, Y., Yan, S., Liu, J., Zhao, Y., Jiang, F., and Lou, H. (2019). TREM2
714 deficiency aggravates alpha-synuclein-induced neurodegeneration and neuroinflammation in
715 Parkinson's disease models. FASEB journal *33*, 12164-12174.
716 Hamada, F.N., Rosenzweig, M., Kang, K., Pulver, S.R., Ghezzi, A., Jegla, T.J., and Garrity, P.A.
717 (2008). An internal thermal sensor controlling temperature preference in Drosophila. Nature
718 *454*, 217-220.

719 Hammond, T.R., Robinton, D., and Stevens, B. (2018). Microglia and the Brain: Complementary
720 Partners in Development and Disease. Annual review of cell and developmental biology *34*,
721 523-544.
722 Han, C., Song, Y., Xiao, H., Wang, D., Franc, N.C., Jan, L.Y., and Jan, Y.N. (2014). Epidermal cells are
723 the primary phagocytes in the fragmentation and clearance of degenerating dendrites in
724 Drosophila. Neuron *81*, 544-560.
725 Hay, B.A., Wolff, T., and Rubin, G.M. (1994). Expression of baculovirus P35 prevents cell death in
726 Drosophila. Development *120*, 2121-2129.
727 Holmes, B.B., DeVos, S.L., Kfoury, N., Li, M., Jacks, R., Yanamandra, K., Ouidja, M.O., Brodsky, F.M.,
728 Marasa, J., Bagchi, D.P.*, et al.* (2013). Heparan sulfate proteoglycans mediate internalization
729 and propagation of specific proteopathic seeds. Proceedings of the National Academy of
730 Sciences of the United States of America *110*, E3138-3147.
731 Hong, S., Beja-Glasser, V.F., Nfonoyim, B.M., Frouin, A., Li, S., Ramakrishnan, S., Merry, K.M., Shi,
732 Q., Rosenthal, A., Barres, B.A.*, et al.* (2016). Complement and microglia mediate early synapse
733 loss in Alzheimer mouse models. Science *352*, 712-716.
734 Hoopfer, E.D., McLaughlin, T., Watts, R.J., Schuldiner, O., O'Leary, D.D., and Luo, L. (2006). Wlds
735 protection distinguishes axon degeneration following injury from naturally occurring
736 developmental pruning. Neuron *50*, 883-895.
737 Jefferis, G.S., Marin, E.C., Stocker, R.F., and Luo, L. (2001). Target neuron prespecification in the
738 olfactory map of Drosophila. Nature *414*, 204-208.
739 Jeon, I., Cicchetti, F., Cisbani, G., Lee, S., Li, E., Bae, J., Lee, N., Li, L., Im, W., Kim, M.*, et al.* (2016).
740 Human-to-mouse prion-like propagation of mutant huntingtin protein. Acta neuropathologica
741 *132*, 577-592.
742 Juhász, G., Hill, J.H., Yan, Y., Sass, M., Baehrecke, E.H., Backer, J.M., and Neufeld, T.P. (2008). The
743 class III PI(3)K Vps34 promotes autophagy and endocytosis but not TOR signaling in
744 Drosophila. The Journal of cell biology *181*, 655-666.

745 Knowles, T.P., Vendruscolo, M., and Dobson, C.M. (2014). The amyloid state and its association with
746 protein misfolding diseases. Nature reviews Molecular cell biology *15*, 384-396.
747 Kosaka, T., and Ikeda, K. (1983). Possible temperature-dependent blockage of synaptic vesicle
748 recycling induced by a single gene mutation in Drosophila. Journal of neurobiology *14*, 207-225.
749 Kreher, S.A., Kwon, J.Y., and Carlson, J.R. (2005). The molecular basis of odor coding in the
750 Drosophila larva. Neuron *46*, 445-456.
751 Lai, S.-L., Awasaki, T., Ito, K., and Lee, T. (2008). Clonal analysis of Drosophila antennal
752 lobe neurons: diverse neuronal architectures in the lateral neuroblast lineage. Development
753 *135*, 2883-2893.
754 Lee, H.-J., Suk, J.-E., Patrick, C., Bae, E.-J., Cho, J.-H., Rho, S., Hwang, D., Masliah, E., and Lee, S.-J.
755 (2010). Direct Transfer of α-Synuclein from Neuron to Astroglia Causes Inflammatory
756 Responses in Synucleinopathies. Journal of Biological Chemistry *285*, 9262-9272.
757 Lee, T., and Luo, L. (1999). Mosaic analysis with a repressible cell marker for studies of gene function
758 in neuronal morphogenesis. Neuron *22*, 451-461.
759 Leyns, C.E.G., Gratuze, M., Narasimhan, S., Jain, N., Koscal, L.J., Jiang, H., Manis, M., Colonna, M.,
760 Lee, V.M.Y., Ulrich, J.D.*, et al.* (2019). TREM2 function impedes tau seeding in neuritic plaques.
761 Nature neuroscience *22*, 1217-1222.
762 Li, Z., Wang, C., Wang, Z., Zhu, C., Li, J., Sha, T., Ma, L., Gao, C., Yang, Y., Sun, Y.*, et al.* (2019).
763 Allele-selective lowering of mutant HTT protein by HTT–LC3 linker compounds. Nature *575*,
764 203-209.
765 Liang, L., Li, Y., Potter, C.J., Yizhar, O., Deisseroth, K., Tsien, R.W., and Luo, L. (2013). GABAergic
766 projection neurons route selective olfactory inputs to specific higher-order neurons. Neuron *79*,
767 917-931.
768 Liddelow, S.A., Guttenplan, K.A., Clarke, L.E., Bennett, F.C., Bohlen, C.J., Schirmer, L., Bennett, M.L.,
769 Munch, A.E., Chung, W.S., Peterson, T.C.*, et al.* (2017). Neurotoxic reactive astrocytes are
770 induced by activated microglia. Nature *541*, 481-487.

771 Lin, D.M., and Goodman, C.S. (1994). Ectopic and increased expression of Fasciclin II alters
772 motoneuron growth cone guidance. Neuron *13*, 507-523.
773 MacDonald, J.M., Beach, M.G., Porpiglia, E., Sheehan, A.E., Watts, R.J., and Freeman, M.R. (2006).
774 The Drosophila cell corpse engulfment receptor Draper mediates glial clearance of severed
775 axons. Neuron *50*, 869-881.
776 MacDonald, M.E., Ambrose, C.M., Duyao, M.P., Myers, R.H., Lin, C., Srinidhi, L., Barnes, G., Taylor,
777 S.A., James, M., Groot, N.*, et al.* (1993). A novel gene containing a trinucleotide repeat that is
778 expanded and unstable on Huntington's disease chromosomes. Cell *72*, 971-983.
779 Marin, E.C., Jefferis, G.S., Komiyama, T., Zhu, H., and Luo, L. (2002). Representation of the glomerular
780 olfactory map in the Drosophila brain. Cell *109*, 243-255.
781 Masliah, E., Rockenstein, E., Adame, A., Alford, M., Crews, L., Hashimoto, M., Seubert, P., Lee, M.,
782 Goldstein, J., Chilcote, T.*, et al.* (2005). Effects of alpha-synuclein immunization in a mouse
783 model of Parkinson's disease. Neuron *46*, 857-868.
784 Masnata, M., Sciacca, G., Maxan, A., Bousset, L., Denis, H.L., Lauruol, F., David, L., Saint-Pierre, M.,
785 Kordower, J.H., Melki, R.*, et al.* (2019). Demonstration of prion-like properties of mutant
786 huntingtin fibrils in both in vitro and in vivo paradigms. Acta neuropathologica *137*, 981-1001.
787 Mezias, C., LoCastro, E., Xia, C., and Raj, A. (2017). Connectivity, not region-intrinsic properties,
788 predicts regional vulnerability to progressive tau pathology in mouse models of disease. Acta
789 neuropathologica communications *5*, 61.
790 Mosca, T.J., and Luo, L. (2014). Synaptic organization of the Drosophila antennal lobe and its
791 regulation by the Teneurins. Elife *3*, e03726.
792 Pearce, M.M., Spartz, E.J., Hong, W., Luo, L., and Kopito, R.R. (2015). Prion-like transmission of
793 neuronal huntingtin aggregates to phagocytic glia in the Drosophila brain. Nature
794 communications *6*, 6768.
795 Pecho-Vrieseling, E., Rieker, C., Fuchs, S., Bleckmann, D., Esposito, M.S., Botta, P., Goldstein, C.,
796 Bernhard, M., Galimberti, I., Muller, M.*, et al.* (2014). Transneuronal propagation of mutant

797 huntingtin contributes to non-cell autonomous pathology in neurons. Nature neuroscience *17*,
798 1064-1072.
799 Potter, C.J., Tasic, B., Russler, E.V., Liang, L., and Luo, L. (2010). The Q system: a repressible binary
800 system for transgene expression, lineage tracing, and mosaic analysis. Cell *141*, 536-548.
801 Poudel, G.R., Harding, I.H., Egan, G.F., and Georgiou-Karistianis, N. (2019). Network spread
802 determines severity of degeneration and disconnection in Huntington's disease. Human brain
803 mapping *40*, 4192-4201.
804 Preisinger, E., Jordan, B.M., Kazantsev, A., and Housman, D. (1999). Evidence for a recruitment and
805 sequestration mechanism in Huntington's disease. Philosophical transactions of the Royal
806 Society of London Series B, Biological sciences *354*, 1029-1034.
807 Pulipparacharuvil, S., Akbar, M.A., Ray, S., Sevrioukov, E.A., Haberman, A.S., Rohrer, J., and Krämer,
808 H. (2005). Drosophila Vps16A is required for trafficking to lysosomes and
809 biogenesis of pigment granules. Journal of cell science *118*, 3663-3673.
810 Ray, A., Speese, S.D., and Logan, M.A. (2017). Glial Draper Rescues Abeta Toxicity in a Drosophila
811 Model of Alzheimer's Disease. The Journal of neuroscience : the official journal of the Society
812 for Neuroscience *37*, 11881-11893.
813 Reiner, A., and Deng, Y.P. (2018). Disrupted striatal neuron inputs and outputs in Huntington's disease.
814 CNS neuroscience & therapeutics *24*, 250-280.
815 Ren, P.H., Lauckner, J.E., Kachirskaia, I., Heuser, J.E., Melki, R., and Kopito, R.R. (2009). Cytoplasmic
816 penetration and persistent infection of mammalian cells by polyglutamine aggregates. Nature
817 cell biology *11*, 219-225.
818 Riabinina, O., Luginbuhl, D., Marr, E., Liu, S., Wu, M.N., Luo, L., and Potter, C.J. (2015). Improved and
819 expanded Q-system reagents for genetic manipulations. Nature methods *12*, 219-222.
820 Riabinina, O., and Potter, C.J. (2016). The Q-System: A Versatile Expression System for Drosophila.
821 Methods in molecular biology *1478*, 53-78.
822 Sathasivam, K., Neueder, A., Gipson, T.A., Landles, C., Benjamin, A.C., Bondulich, M.K., Smith, D.L.,
823 Faull, R.L., Roos, R.A., Howland, D.*, et al.* (2013). Aberrant splicing of HTT generates the

824 pathogenic exon 1 protein in Huntington disease. Proceedings of the National Academy of
825 Sciences of the United States of America *110*, 2366-2370.
826 Schafer, D.P., Lehrman, E.K., Kautzman, A.G., Koyama, R., Mardinly, A.R., Yamasaki, R., Ransohoff,
827 R.M., Greenberg, M.E., Barres, B.A., and Stevens, B. (2012). Microglia sculpt postnatal neural
828 circuits in an activity and complement-dependent manner. Neuron *74*, 691-705.
829 Sepp, K.J., Schulte, J., and Auld, V.J. (2001). Peripheral glia direct axon guidance across the
830 CNS/PNS transition zone. Developmental biology *238*, 47-63.
831 Sharma, M., and Subramaniam, S. (2019). Rhes travels from cell to cell and transports Huntington
832 disease protein via TNT-like protrusion. The Journal of cell biology *218*, 1972-1993.
833 Stepensky, D. (2007). FRETcalc plugin for calculation of FRET in non-continuous intracellular
834 compartments. Biochemical and biophysical research communications *359*, 752-758.
835 Stocker, R.F., Heimbeck, G., Gendre, N., and de Belle, J.S. (1997). Neuroblast ablation in Drosophila
836 P[GAL4] lines reveals origins of olfactory interneurons. Journal of neurobiology *32*, 443-456.
837 Stockinger, P., Kvitsiani, D., Rotkopf, S., Tirian, L., and Dickson, B.J. (2005). Neural circuitry that
838 governs Drosophila male courtship behavior. Cell *121*, 795-807.
839 Sweeney, S.T., Broadie, K., Keane, J., Niemann, H., and O'Kane, C.J. (1995). Targeted expression of
840 tetanus toxin light chain in Drosophila specifically eliminates synaptic transmission and causes
841 behavioral defects. Neuron *14*, 341-351.
842 Tabrizi, S.J., Leavitt, B.R., Landwehrmeyer, G.B., Wild, E.J., Saft, C., Barker, R.A., Blair, N.F.,
843 Craufurd, D., Priller, J., Rickards, H.*, et al.* (2019). Targeting Huntingtin Expression in Patients
844 with Huntington's Disease. The New England journal of medicine *380*, 2307-2316.
845 Tran, H.T., Chung, C.H., Iba, M., Zhang, B., Trojanowski, J.Q., Luk, K.C., and Lee, V.M. (2014). Alpha-
846 synuclein immunotherapy blocks uptake and templated propagation of misfolded alpha-
847 synuclein and neurodegeneration. Cell reports *7*, 2054-2065.
848 Tremblay, M.E., Zettel, M.L., Ison, J.R., Allen, P.D., and Majewska, A.K. (2012). Effects of aging and
849 sensory loss on glial cells in mouse visual and auditory cortices. Glia *60*, 541-558.

850 Trevino, R.S., Lauckner, J.E., Sourigues, Y., Pearce, M.M., Bousset, L., Melki, R., and Kopito, R.R.
851 (2012). Fibrillar structure and charge determine the interaction of polyglutamine protein
852 aggregates with the cell surface. The Journal of biological chemistry *287*, 29722-29728.
853 Vaquer-Alicea, J., and Diamond, M.I. (2019). Propagation of Protein Aggregation in Neurodegenerative
854 Diseases. Annual review of biochemistry *88*, 785-810.
855 Victoria, G.S., Arkhipenko, A., Zhu, S., Syan, S., and Zurzolo, C. (2016). Astrocyte-to-neuron
856 intercellular prion transfer is mediated by cell-cell contact. Scientific reports *6*, 20762.
857 Wang, N., Gray, M., Lu, X.-H., Cantle, J.P., Holley, S.M., Greiner, E., Gu, X., Shirasaki, D., Cepeda, C.,
858 Li, Y.*, et al.* (2014). Neuronal targets for reducing mutant huntingtin expression to ameliorate
859 disease in a mouse model of Huntington's disease. Nature medicine *20*, 536-541.
860 Weinhard, L., di Bartolomei, G., Bolasco, G., Machado, P., Schieber, N.L., Neniskyte, U., Exiga, M.,
861 Vadisiute, A., Raggioli, A., Schertel, A.*, et al.* (2018). Microglia remodel synapses by
862 presynaptic trogocytosis and spine head filopodia induction. Nature communications *9*, 1228.
863 Weiss, K.R., Kimura, Y., Lee, W.C., and Littleton, J.T. (2012). Huntingtin aggregation kinetics and their
864 pathological role in a Drosophila Huntington's disease model. Genetics *190*, 581-600.
865 Wilton, D.K., Dissing-Olesen, L., and Stevens, B. (2019). Neuron-Glia Signaling in Synapse Elimination.
866 Annual review of neuroscience *42*, 107-127.
867 Wu, J.W., Hussaini, S.A., Bastille, I.M., Rodriguez, G.A., Mrejeru, A., Rilett, K., Sanders, D.W., Cook,
868 C., Fu, H., Boonen, R.A.*, et al.* (2016). Neuronal activity enhances tau propagation and tau
869 pathology in vivo. Nature neuroscience *19*, 1085-1092.
870 Wyss-Coray, T., Loike, J.D., Brionne, T.C., Lu, E., Anankov, R., Yan, F., Silverstein, S.C., and
871 Husemann, J. (2003). Adult mouse astrocytes degrade amyloid-beta in vitro and in situ. Nature
872 medicine *9*, 453-457.
873 Yanamandra, K., Kfoury, N., Jiang, H., Mahan, T.E., Ma, S., Maloney, S.E., Wozniak, D.F., Diamond,
874 M.I., and Holtzman, D.M. (2013). Anti-tau antibodies that block tau aggregate seeding in vitro
875 markedly decrease pathology and improve cognition in vivo. Neuron *80*, 402-414.

876 Yun, S.P., Kam, T.I., Panicker, N., Kim, S., Oh, Y., Park, J.S., Kwon, S.H., Park, Y.J., Karuppagounder,
877 S.S., Park, H.*, et al.* (2018). Block of A1 astrocyte conversion by microglia is neuroprotective in
878 models of Parkinson's disease. Nature medicine *24*, 931-938.
879 Zeineddine, R., Pundavela, J.F., Corcoran, L., Stewart, E.M., Do-Ha, D., Bax, M., Guillemin, G., Vine,
880 K.L., Hatters, D.M., Ecroyd, H.*, et al.* (2015). SOD1 protein aggregates stimulate
881 macropinocytosis in neurons to facilitate their propagation. Molecular neurodegeneration *10*, 57.
882 Zhao, Y., Wu, X., Li, X., Jiang, L.L., Gui, X., Liu, Y., Sun, Y., Zhu, B., Pina-Crespo, J.C., Zhang, M.*, et*
883 *al.* (2018). TREM2 Is a Receptor for beta-Amyloid that Mediates Microglial Function. Neuron *97*,
884 1023-1031.

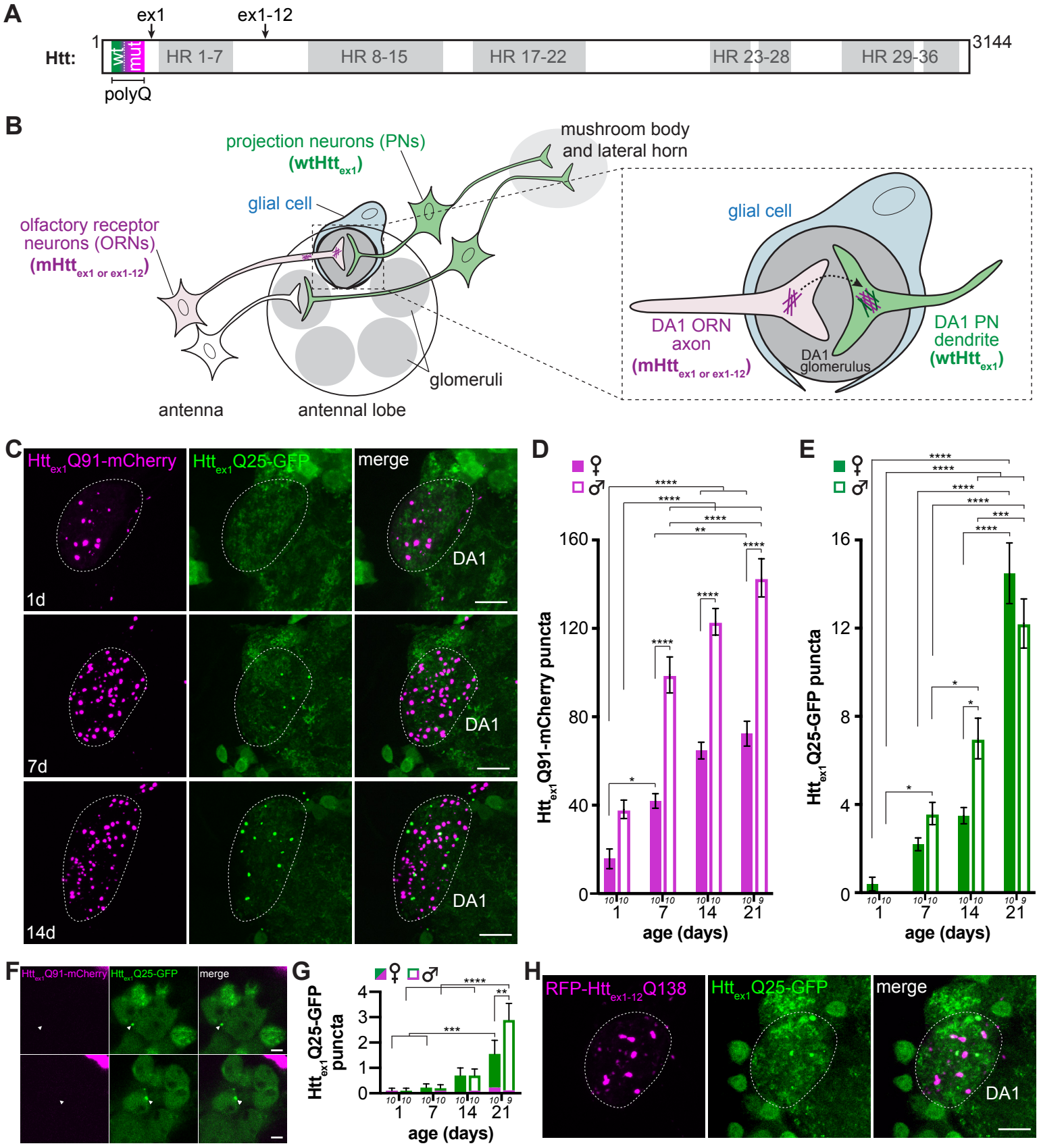
A
ex1
ex1-12
Htt:
1
3144
wt
mut
HR 1-7
HR 8-15
HR 17-22
HR 23-28
HR 29-36
polyQ
B
projection neurons (PNs)
(wtHtt$_{ex1}$)
mushroom body
and lateral horn
glial cell
olfactory receptor
neurons (ORNs)
(mHtt$_{ex1\ or\ ex1-12}$)
glomeruli
antenna
antennal lobe
glial cell
DA1 ORN
axon
(mHtt$_{ex1\ or\ ex1-12}$)
DA1
glomerulus
DA1 PN
dendrite
(wtHtt$_{ex1}$)
C
Htt$_{ex1}$Q91-mCherry
Htt$_{ex1}$Q25-GFP
merge
DA1
1d
7d
14d
D
♀
♂
Htt$_{ex1}$Q91-mCherry puncta
age (days)
E
Htt$_{ex1}$Q25-GFP puncta
age (days)
F
Htt$_{ex1}$Q91-mCherry
Htt$_{ex1}$Q25-GFP
merge
G
Htt$_{ex1}$Q25-GFP puncta
age (days)
H
RFP-Htt$_{ex1-12}$Q138
Htt$_{ex1}$Q25-GFP
merge
DA1

Figure 1. $mHtt_{ex1}$ or $mHtt_{ex1-12}$ aggregates generated in presynaptic ORNs nucleate the aggregation of $wtHtt_{ex1}$ in postsynaptic PNs. (A) Cartoon depiction of full-length human Htt (3144 amino acids). The majority of the Htt protein is composed of 36 HEAT repeat domains (HR, gray regions). The variable-length polyQ region (green/magenta) is located near the N-terminus, with the pathogenic threshold (~Q37) indicated by the white dotted line. The C-termini of two N-terminal pathogenic fragments used in this study (ex1 and ex1-12) are indicated by arrows. (B) Diagram illustrating our overall experimental approach. In the fly olfactory system, primary ORNs synapse with secondary PNs in discrete regions of the antennal lobe known as glomeruli (gray circles). PNs send their axons into higher brain centers (mushroom body and/or lateral horn). Several glial cell types also reside in or near the antennal lobe, including Draper-expressing glia whose processes ensheath individual glomeruli in the antennal lobe. To examine spreading of mHtt aggregates between synaptically-connected ORNs and PNs, we generated transgenic flies that express mHtt fragments (*QUAS-Htt_{ex1}Q91-mCherry* or *QUAS-RFP-Htt_{ex1-12}Q138*) in DA1 ORNs using the *Or67d-QF* driver and *UAS-Htt_{ex1}Q25-GFP* in DA1 PNs using *GH146-Gal4*, which labels ~60% of PNs. Inset: Transfer of mHtt aggregates between ORNs and PNs was assessed by monitoring the solubility of Htt_{ex1}Q25-GFP in PN dendrites and cell bodies and co-localization of GFP+ puncta with mCherry/RFP+ mHtt aggregates. (C) Maximum intensity z-projections of the DA1 glomerulus from adult males at the indicated ages expressing Htt_{ex1}Q91-mCherry in DA1 ORNs (*magenta*) and Htt_{ex1}Q25-GFP in GH146+ PNs (*green*). Approximate boundaries of the DA1 glomerulus are indicated by the white dotted line. (D) and (E) Quantification of Htt_{ex1}Q91-mCherry (D) and Htt_{ex1}Q25-GFP (E) puncta in the DA1 glomerulus of adult female (*solid bars*) or male (*open bars*) flies at the indicated ages. (F) Single z-slice images showing Htt_{ex1}Q25-GFP puncta (*arrowheads*) in lateral PN soma from 21 day-old males with the same genotype as in (C-E). (G) Quantification of Htt_{ex1}Q25-GFP puncta detected in PN soma in female (*solid bars*) and male (*open bars*) flies at the indicated ages. Puncta that were GFP+ only and those that were both GFP+ and mCherry+ at each age are indicated by stacked green and magenta bars, respectively. (H) Maximum intensity z-projections from a 7 day-old adult female expressing RFP-Htt_{ex1-12}Q138 in DA1 ORNs and Htt_{ex1}Q25-GFP in GH146+ PNs. In (D), (E), and (G), error bars indicate ± SEM; *n* is indicated below each data set. Statistical comparisons made for females or males at different ages were calculated using two-way ANOVA with Tukey's multiple comparisons tests, and Student's *t*-test was used for pairwise comparisons between age-matched females and males (*$p < 0.05$, **$p < 0.01$, ***$p < 0.001$, or ****$p < 0.0001$). Scale bars = 10 μm in (C) and (H), and 5 μm in (F).

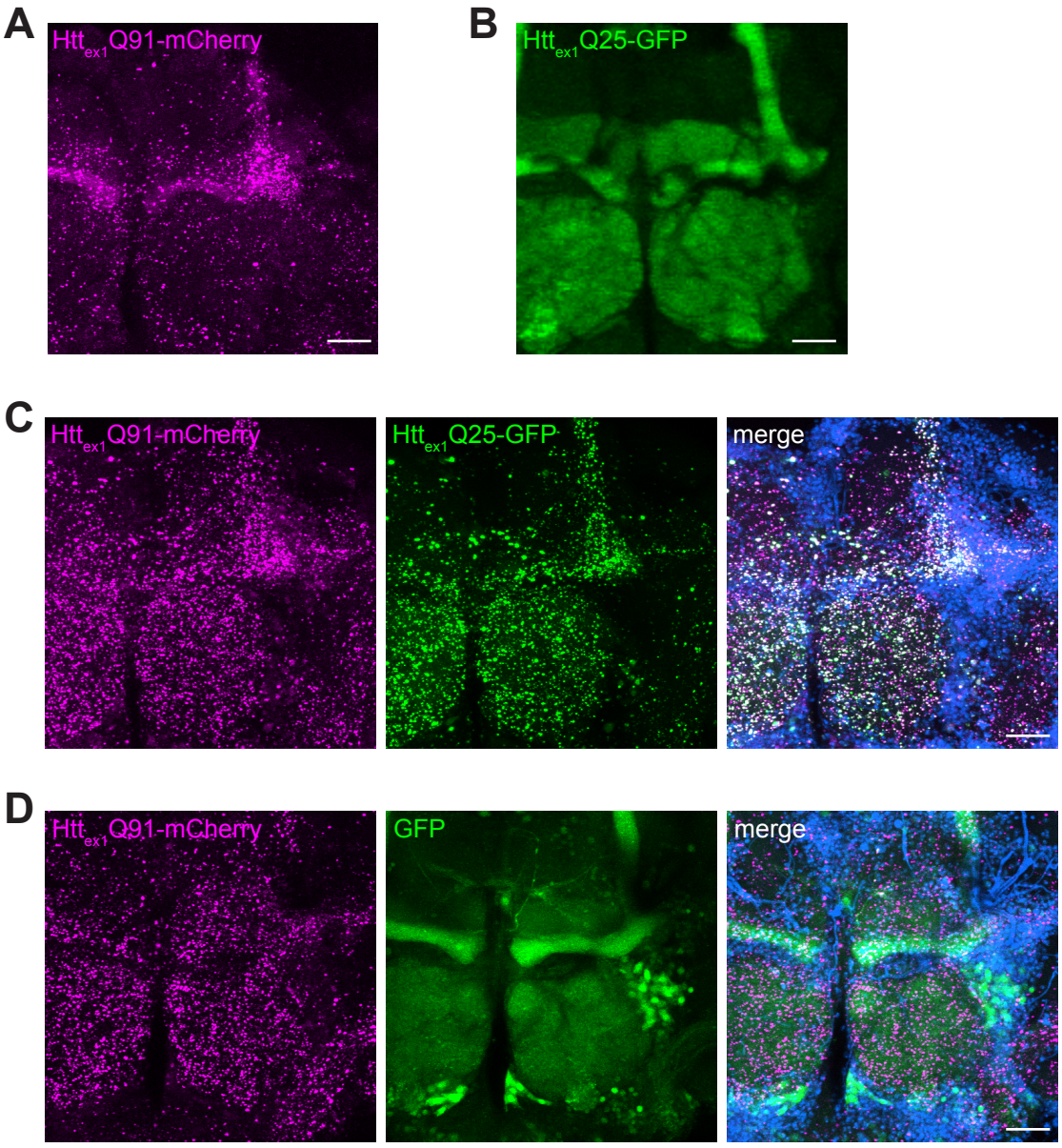

Figure 1 – figure supplement 1. mHtt$_{ex1}$ aggregates induce prion-like conversion of wtHtt$_{ex1}$ in neurons. (A and B) Maximum intensity z-projections of 7 day-old adult female brains expressing either Htt$_{ex1}$Q91-mCherry (A) or Htt$_{ex1}$Q25-GFP (B) using pan-neuronal *elav[C155]-Gal4*. (C) and (D) Co-expression of Htt$_{ex1}$Q91-mCherry and Htt$_{ex1}$Q25-GFP (C) or GFP (D) in all neurons with *elav[C155]-Gal4*. Merged images include DAPI signal (blue) to indicate nuclei. Scale bars = 10 μm in all images.

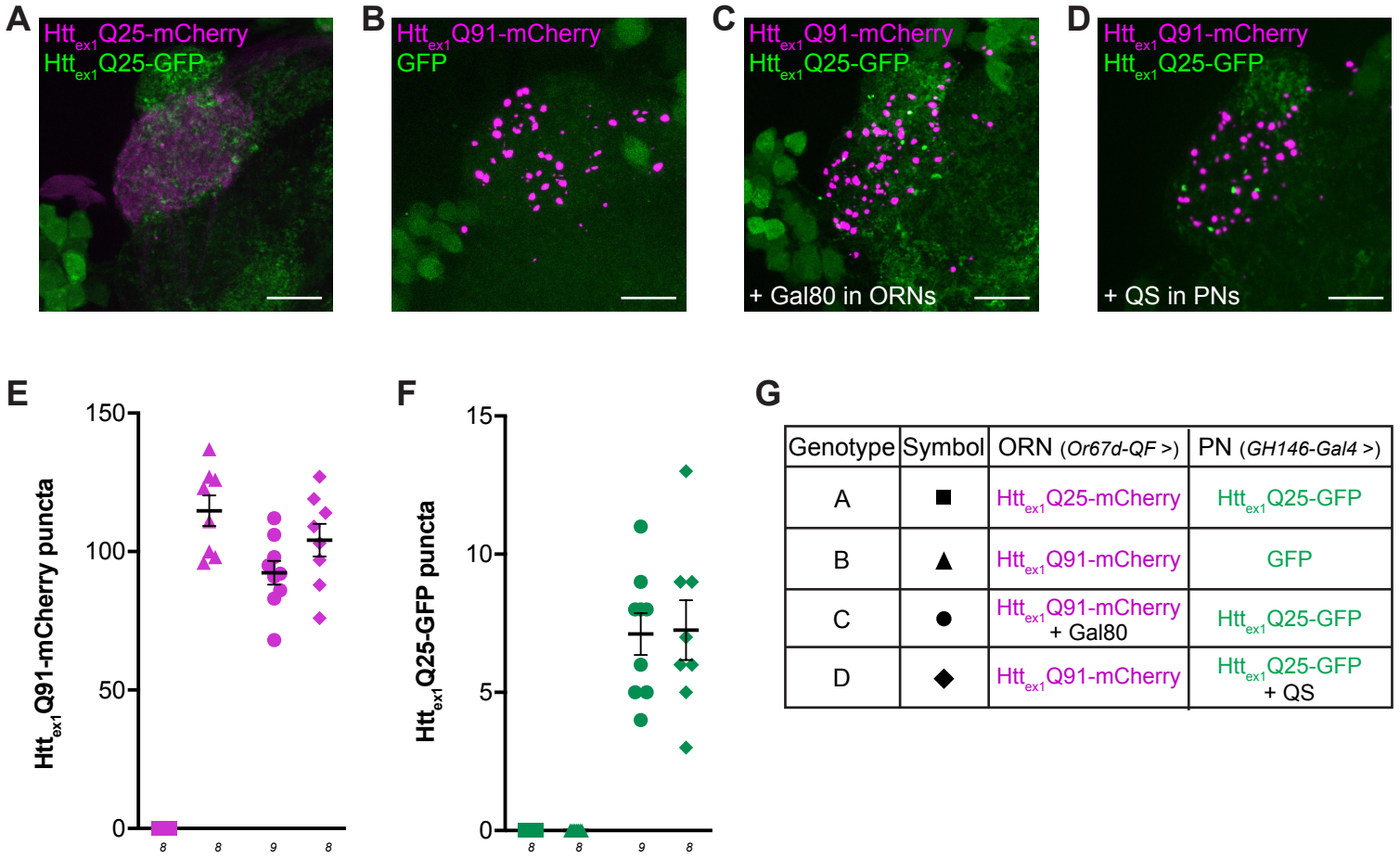

Genotype	Symbol	ORN (*Or67d-QF* >)	PN (*GH146-Gal4* >)
A	■	Htt$_{ex1}$Q25-mCherry	Htt$_{ex1}$Q25-GFP
B	▲	Htt$_{ex1}$Q91-mCherry	GFP
C	●	Htt$_{ex1}$Q91-mCherry + Gal80	Htt$_{ex1}$Q25-GFP
D	◆	Htt$_{ex1}$Q91-mCherry	Htt$_{ex1}$Q25-GFP + QS

Figure 1 – figure supplement 2. Controls for spreading of mHtt$_{ex1}$ aggregates between synaptically-connected ORNs and PNs. (A-D) Maximum-intensity z-projections of the DA1 glomerulus from 10 day-old adults expressing (A) Htt$_{ex1}$Q25-mCherry in DA1 ORNs and Htt$_{ex1}$Q25-GFP in GH146+ PNs, (B) Htt$_{ex1}$Q91-mCherry in DA1 ORNs and GFP in PNs, (C) Htt$_{ex1}$Q91-mCherry together with Gal80 in DA1 ORNs and Htt$_{ex1}$Q25-GFP in GH146+ PNs, and (D) Htt$_{ex1}$Q91-mCherry in DA1 ORNs and Htt$_{ex1}$Q25-GFP together with QS in GH146+ PNs. Scale bars = 10 μm. (E and F) Quantification of mCherry+ (E) and GFP+ (F) aggregates for all genotypes shown in (A-D). Horizontal bars indicate mean, and error bars indicate ± SEM; n ≥ 8. (G) Table summarizing genotypes and graph symbols displayed in (A-F).

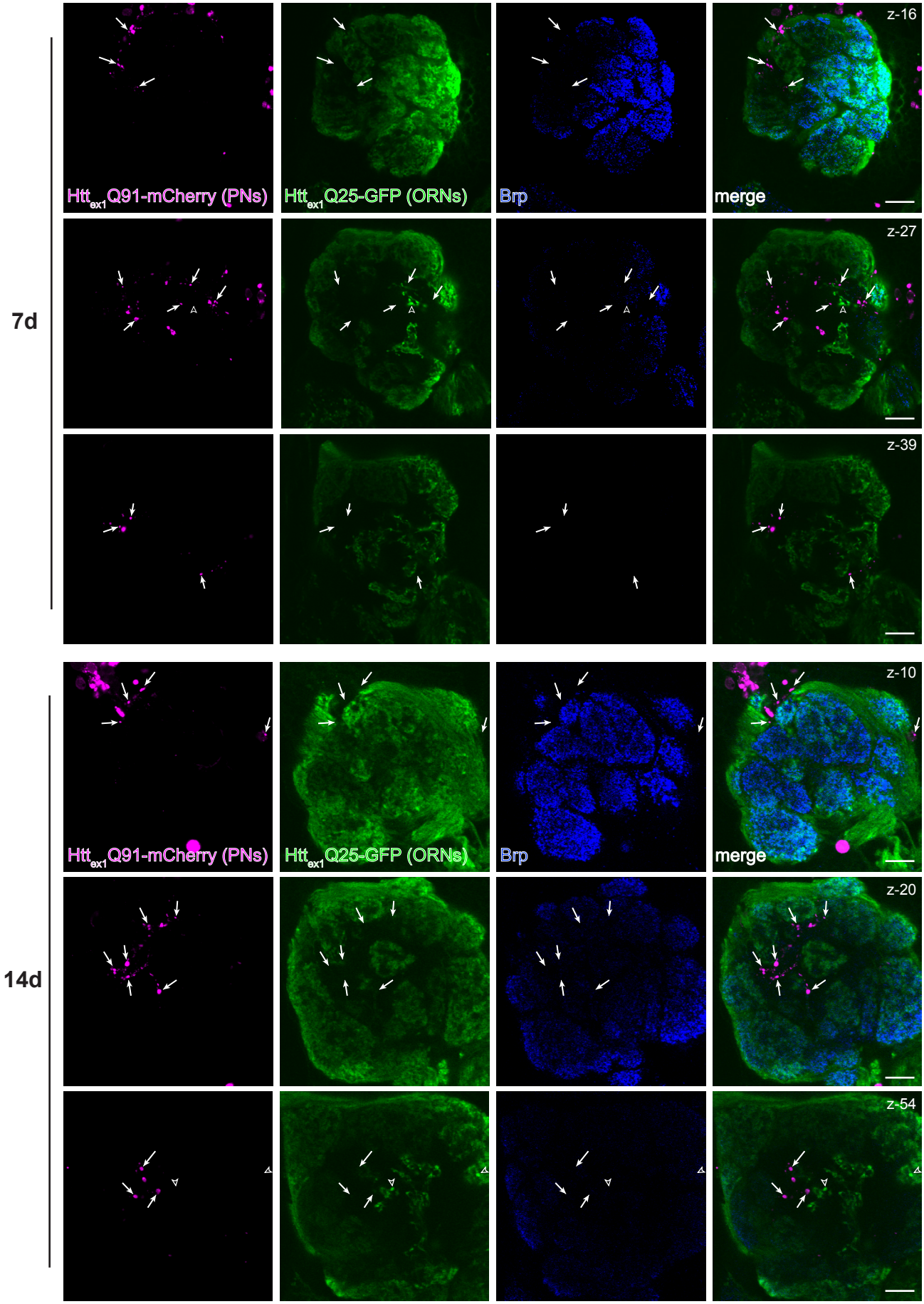
7d
14d
Htt$_{ex1}$Q91-mCherry (PNs)
Htt$_{ex1}$Q25-GFP (ORNs)
Brp
merge
z-16
z-27
z-39
z-10
z-20
z-54

Figure 1 – figure supplement 3. $mHtt_{ex1}$ aggregates do not transfer retrogradely from PNs to ORNs. Single confocal z-slices of the antennal lobe from 7 (*top 3 rows*) and 14 (*bottom 3 rows*) day-old adults expressing Htt_{ex1}Q91-mCherry in ~60% of PNs using *GH146-QF* and Htt_{ex1}Q25-GFP in all ORNs using *pebbled-Gal4*. The brains were immunostained with antibodies against mCherry (*magenta*), GFP (*green*), and the neuropil marker Bruchpilot (Brp; *blue*). Individual mCherry+ puncta are indicated by solid white arrows and punctate GFP+ structures by open arrowheads. Scale bars = 10 μm, relative z-positions in each confocal stack are indicated in upper right of merged images.

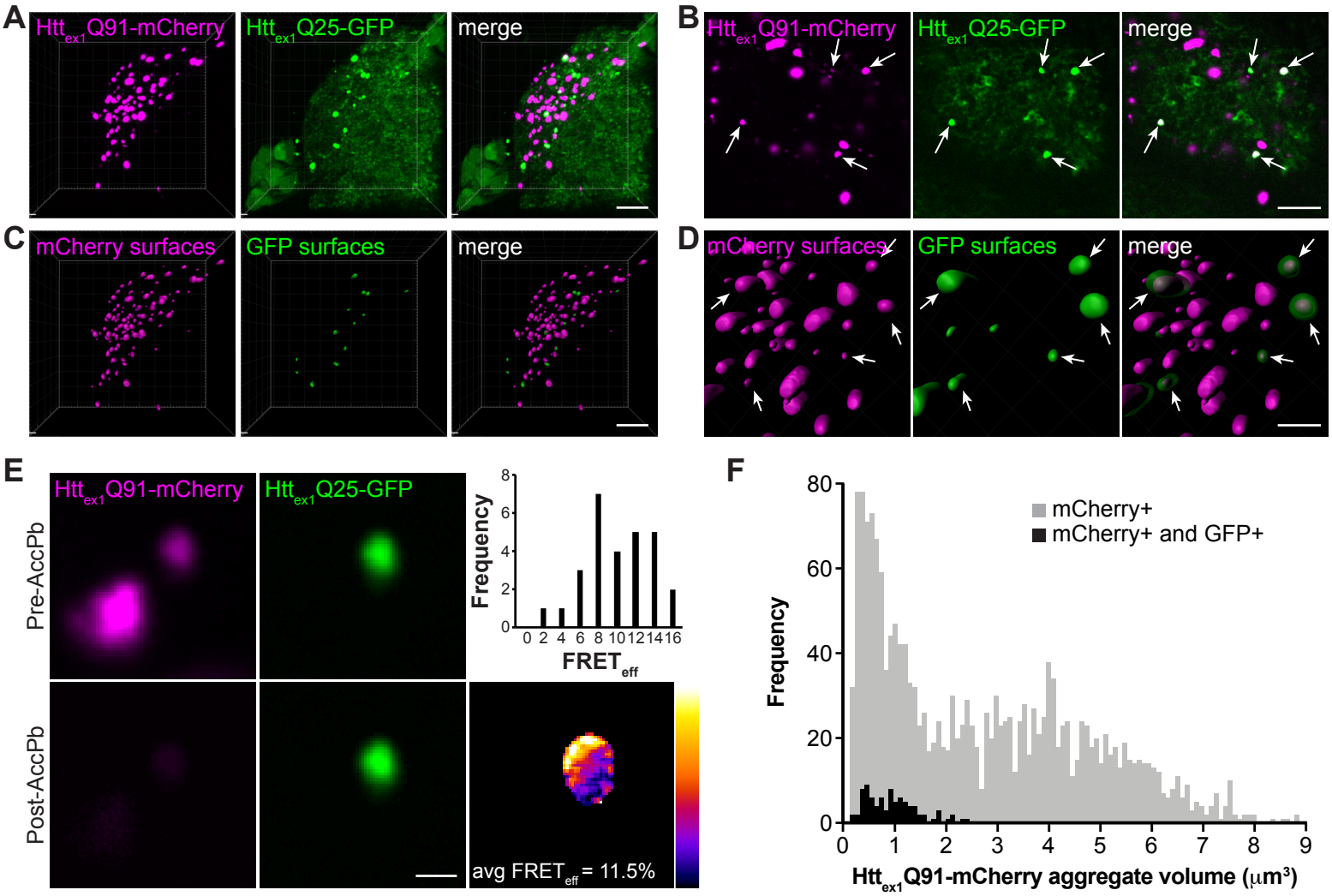

Figure 2. Features of induced Htt$_{ex1}$Q25-GFP aggregates in PNs. (A) Three-dimensional rendering of the DA1 glomerulus from a 14 day-old adult male expressing Htt$_{ex1}$Q91-mCherry in DA1 ORNs and Htt$_{ex1}$Q25-GFP in GH146+ PNs. (B) A single confocal slice from an adult male with the same genotype as in (A) showing four induced Htt$_{ex1}$Q25-GFP aggregates and associated Htt$_{ex1}$Q91-mCherry signals (arrows). (C and D) Volumetric surface renderings of the raw confocal data shown in (A). Thresholding was adjusted in each channel to ensure that the majority of Htt$_{ex1}$Q91-mCherry puncta were identified as individual objects (mCherry surfaces) and induced Htt$_{ex1}$Q25-GFP aggregates were identified as objects distinguishable from surrounding diffuse signal (GFP surfaces). In the higher magnification view shown in (D), GFP surfaces were set at 50% transparency in the merged image so that co-localized mCherry surfaces are visible. Five individual Htt$_{ex1}$Q91-mCherry + Htt$_{ex1}$Q25-GFP co-localized aggregates are indicated by arrows. (E) A single mCherry+ and GFP+ aggregate before ("Pre-AccPb") and after ("Post-AccPb") photobleaching of the mCherry acceptor fluorophore. A larger mCherry-only aggregate is also shown in the image as a control. Pixel-by-pixel FRET efficiency (FRET$_{eff}$) is shown as a heat map image (*bottom right*; colorbar scale to right of image), calculated using the equation $(GFP_{final} - GFP_{initial})/GFP_{final}$. Average FRET$_{eff}$ for this aggregate was 11.5%. Average FRET$_{eff}$ values for all induced Htt$_{ex1}$Q25-GFP aggregates tested by this method are shown in the histogram above the FRET$_{eff}$ image (n = 28). (F) Distribution of volumes for all mCherry+ aggregates (*gray bars*; n = 1792) or mCherry+ aggregate seeds that co-localized with induced Htt$_{ex1}$Q25-GFP aggregates (*black bars*; n = 100) detected in the DA1 glomerulus of 7 and 14 day-old adult flies with the same genotype as in (A-E). Scale bars = 10 μm (A and C), 5 μm (B), 2 μm (D), and 1 μm (E).

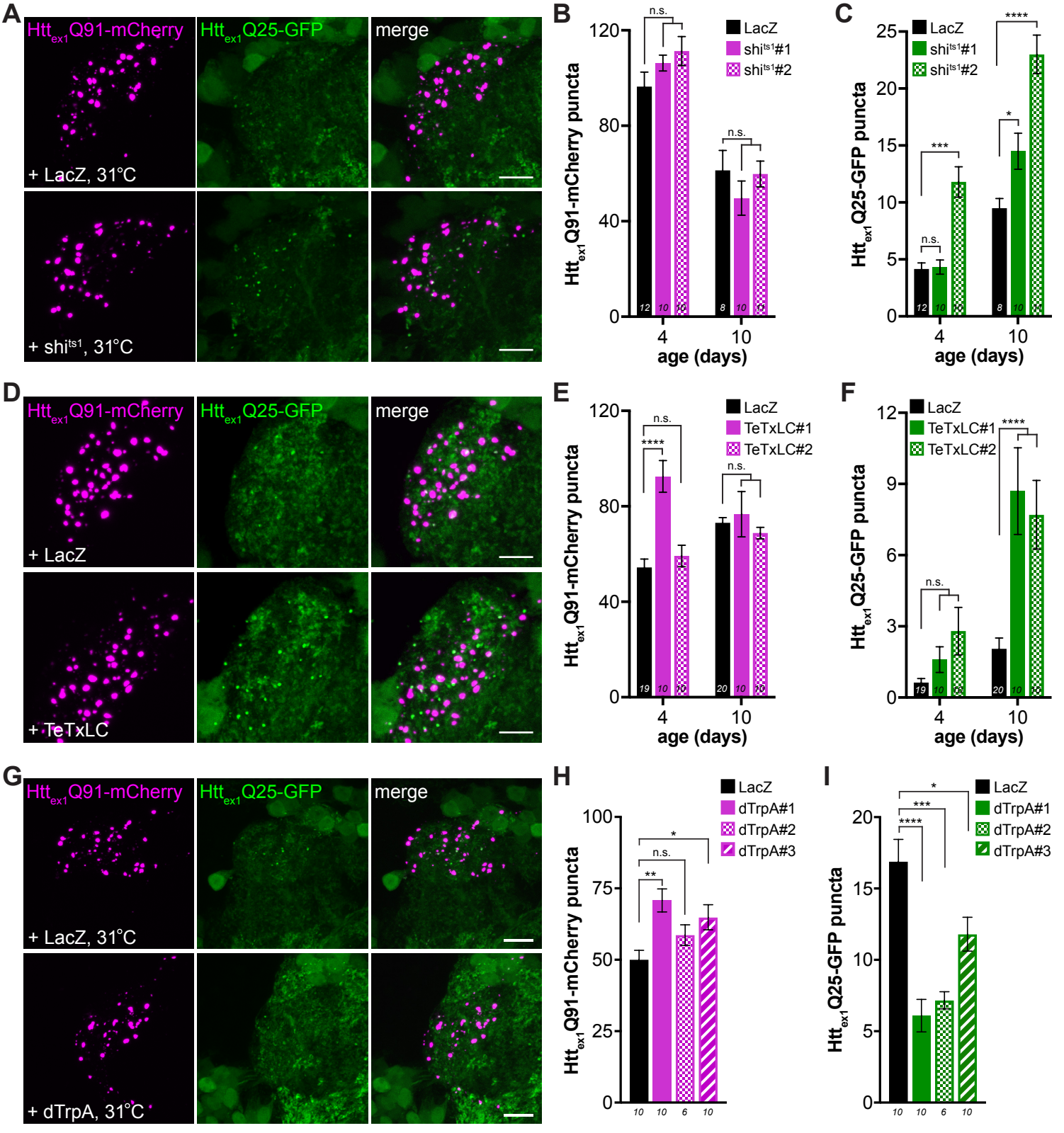
A
Htt$_{ex1}$Q91-mCherry
Htt$_{ex1}$Q25-GFP
merge
+ LacZ, 31°C
+ shi^{ts1}, 31°C
B
Htt$_{ex1}$Q91-mCherry puncta
LacZ
shi^{ts1}#1
shi^{ts1}#2
n.s.
age (days)
C
Htt$_{ex1}$Q25-GFP puncta
****
***
*
n.s.
D
+ LacZ
+ TeTxLC
E
TeTxLC#1
TeTxLC#2
F
G
+ dTrpA, 31°C
H
dTrpA#1
dTrpA#2
dTrpA#3
I

Figure 3. mHtt$_{ex1}$ aggregate transfer from ORNs to synaptically-connected PNs is inversely correlated with presynaptic activity. (A) Maximum-intensity z-projections of the DA1 glomerulus from 10 day-old adult males co-expressing Htt$_{ex1}$Q91-mCherry with LacZ or shi^{ts1} in DA1 ORNs and also expressing Htt$_{ex1}$Q25-GFP in GH146+ PNs. Flies were shifted from the permissive temperature (18°C) to the restrictive temperature (31°C) upon eclosion. (B) and (C) Quantification of Htt$_{ex1}$Q91-mCherry (B) and Htt$_{ex1}$Q25-GFP (C) puncta in the DA1 glomerulus of 4 or 10 day-old adult males expressing LacZ or shi^{ts1} in ORNs using two independent *QUAS-shi^{ts1}* lines. (D) Maximum-intensity z-projections of the DA1 glomerulus from 10 day-old males co-expressing Htt$_{ex1}$Q91-mCherry with LacZ or TeTxLC in DA1 ORNs and expressing Htt$_{ex1}$Q25-GFP in GH146+ PNs. (E) and (F) Quantification of Htt$_{ex1}$Q91-mCherry (E) and Htt$_{ex1}$Q25-GFP (F) puncta in the DA1 glomerulus of 4 or 10 day-old adult males expressing LacZ or TeTxLC in ORNs using two independent *QUAS-TeTxLC* lines. (G) Maximum-intensity z-projections of the DA1 glomerulus from 7 day-old adult females co-expressing Htt$_{ex1}$Q91-mCherry with LacZ or dTrpA in DA1 ORNs and expressing Htt$_{ex1}$Q25-GFP in GH146+ PNs. dTrpA-expressing neurons were activated by shifting the adults from 25°C to 31°C upon eclosion. (H) and (I) Quantification of Htt$_{ex1}$Q91-mCherry (H) and Htt$_{ex1}$Q25-GFP (I) puncta in the DA1 glomerulus of 7 day-old females expressing LacZ or dTrpA in ORNs using three independent *QUAS-dTrpA* lines. For quantifications shown in (B), (C), (D), (E), (H), and (I), error bars indicate ± SEM; *n* is indicated for each data set. *$p < 0.05$, **$p < 0.01$, ***$p < 0.001$, ****$p < 0.0001$, or n.s. = not significant by two-way ANOVA with Sidak's multiple comparisons tests. Scale bars = 10 μm in all images.

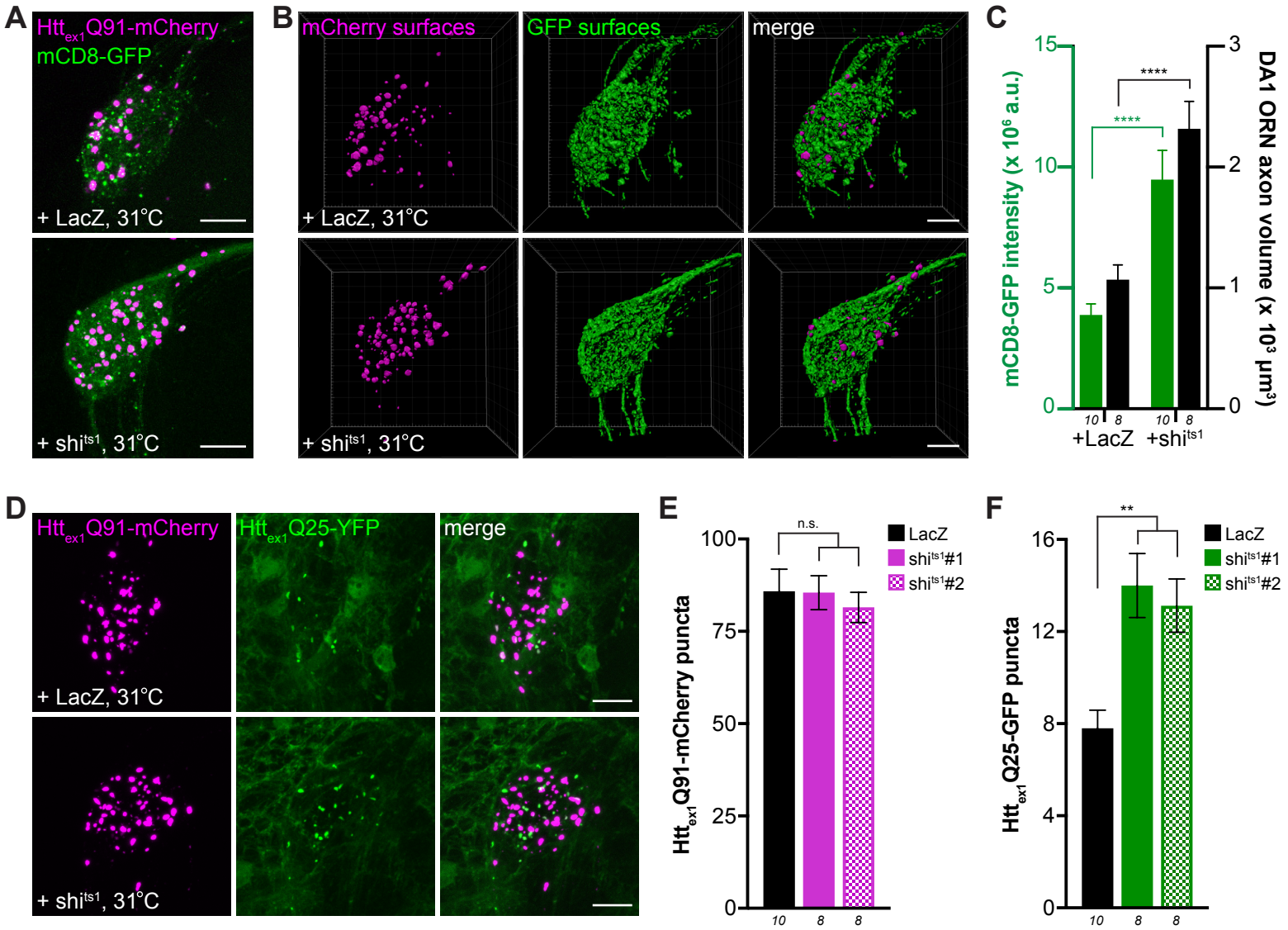

Figure 4. Inhibition of endocytosis increases mHtt$_{ex1}$-expressing ORN axon volume and enhances transfer of neuronal mHtt$_{ex1}$ aggregates to glia. (A) Maximum-intensity z-projections of the DA1 glomerulus from 10 day-old females co-expressing Htt$_{ex1}$Q91-mCherry, mCD8-GFP, and either LacZ or shi^{ts1} in DA1 ORNs. Adult flies were shifted from 18°C to 31°C upon eclosion. (B) Volumetric surface renderings generated for Htt$_{ex1}$Q91-mCherry and mCD8-GFP signals from the same confocal stacks shown in (A). (C) Quantification of mCD8-GFP intensity (*left y-axis, green*) and DA1 ORN axon volume (*right y-axis, black*) in the DA1 glomerulus of 10 day-old adult females expressing LacZ or shi^{ts1} together with Htt$_{ex1}$Q91-mCherry and mCD8-GFP in DA1 ORNs. a.u. = arbitrary units. (D) Maximum-intensity z-projections of the DA1 glomerulus from 5-6 day-old males co-expressing Htt$_{ex1}$Q91-mCherry with either LacZ or shi^{ts1} in DA1 ORNs and expressing Htt$_{ex1}$Q25-YFP in all glia using *repo-Gal4*. Adult flies of each genotype were shifted from 18°C to the restrictive temperature (31°C) upon eclosion. (E and F) Quantification of Htt$_{ex1}$Q91-mCherry (E) and Htt$_{ex1}$Q25-YFP (F) puncta in the DA1 glomerulus of 5-6 day-old males expressing LacZ or shi^{ts1} in ORNs using two independent *QUAS-shi^{ts1}* lines. For quantifications shown in (C), (E), and (F), error bars indicate ± SEM; *n* is indicated below each data set. **$p < 0.01$, ****$p < 0.0001$, or n.s. = not significant by two-way ANOVA with Sidak's multiple comparisons tests in (C) and by one-way ANOVA with Tukey's multiple comparisons tests in (E) and (F). Scale bars = 10 µm in all images.

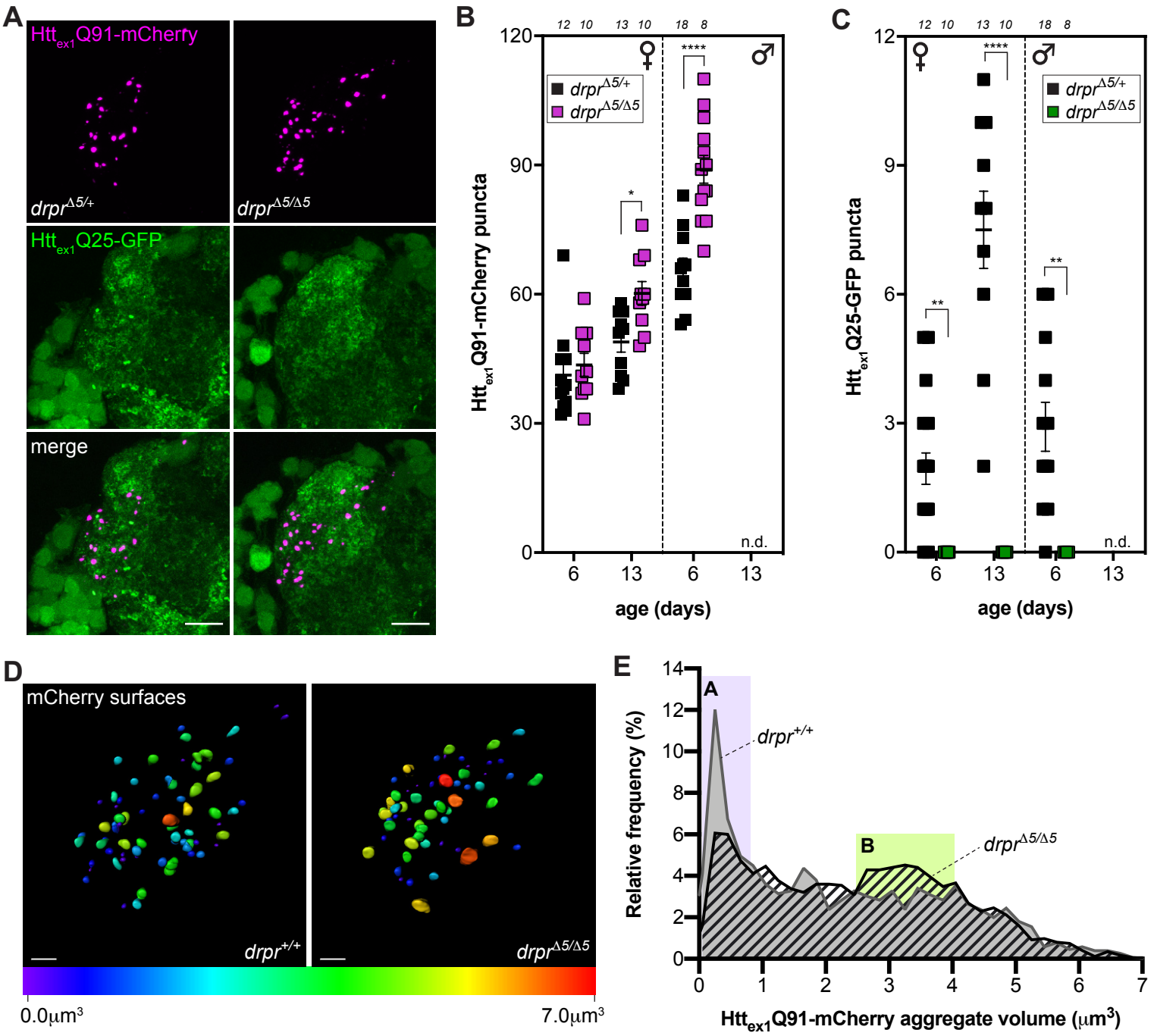

Figure 5. Draper is required for mHtt$_{ex1}$ aggregate transfer from presynaptic ORNs to postsynpatic PNs and regulates neuronal mHtt$_{ex1}$ aggregate size. (A) Maximum-intensity z-projections of the DA1 glomerulus from 13 day-old adult females expressing Htt$_{ex1}$Q91-mCherry in DA1 ORNs and Htt$_{ex1}$Q25-GFP in GH146+ PNs and either heterozygous (*drpr*$^{\Delta5/+}$) or homozygous (*drpr*$^{\Delta5/\Delta5}$) for the *drpr*$^{\Delta5}$ null allele. Scale bars = 10 μm. (B and C) Numbers of Htt$_{ex1}$Q91-mCherry (B) or Htt$_{ex1}$Q25-GFP (C) puncta in the DA1 glomerulus of female or male *drpr*$^{\Delta5/+}$ or *drpr*$^{\Delta5/\Delta5}$ flies. Each symbol represents quantification for an individual DA1 glomerulus. Horizontal bars indicate means, and error bars indicate ± SEM; *n* is shown above each data set. *p < 0.05, **p < 0.01, or ****p < 0.0001 by two-way ANOVA with Tukey's multiple comparisons tests. "n.d." = not determined, as *drpr*$^{\Delta5/\Delta5}$ males did not survive to 13 days old. (D) Three-dimensional rendering of mCherry+ surfaces identified in the DA1 glomerulus of 7 day-old *drpr*$^{+/+}$ or *drpr*$^{\Delta5/\Delta5}$ females expressing Htt$_{ex1}$Q91-mCherry in DA1 ORNs. Colors indicate aggregate volume according to the colorbar scale below the images. Scale bars = 5 μm. (E) Distribution of volumes calculated for all mCherry+ aggregates in 7 day-old *drpr*$^{+/+}$ (*gray line and fill*; *n* = 1556) or *drpr*$^{\Delta5/\Delta5}$ (*black line and striped fill*; *n* = 1749) male and female flies. Purple and green shading indicate smaller- ("A") and larger-sized ("B") aggregate subpopulations, respectively, that experienced a shift in abundance between wild-type and *drpr*-null animals.

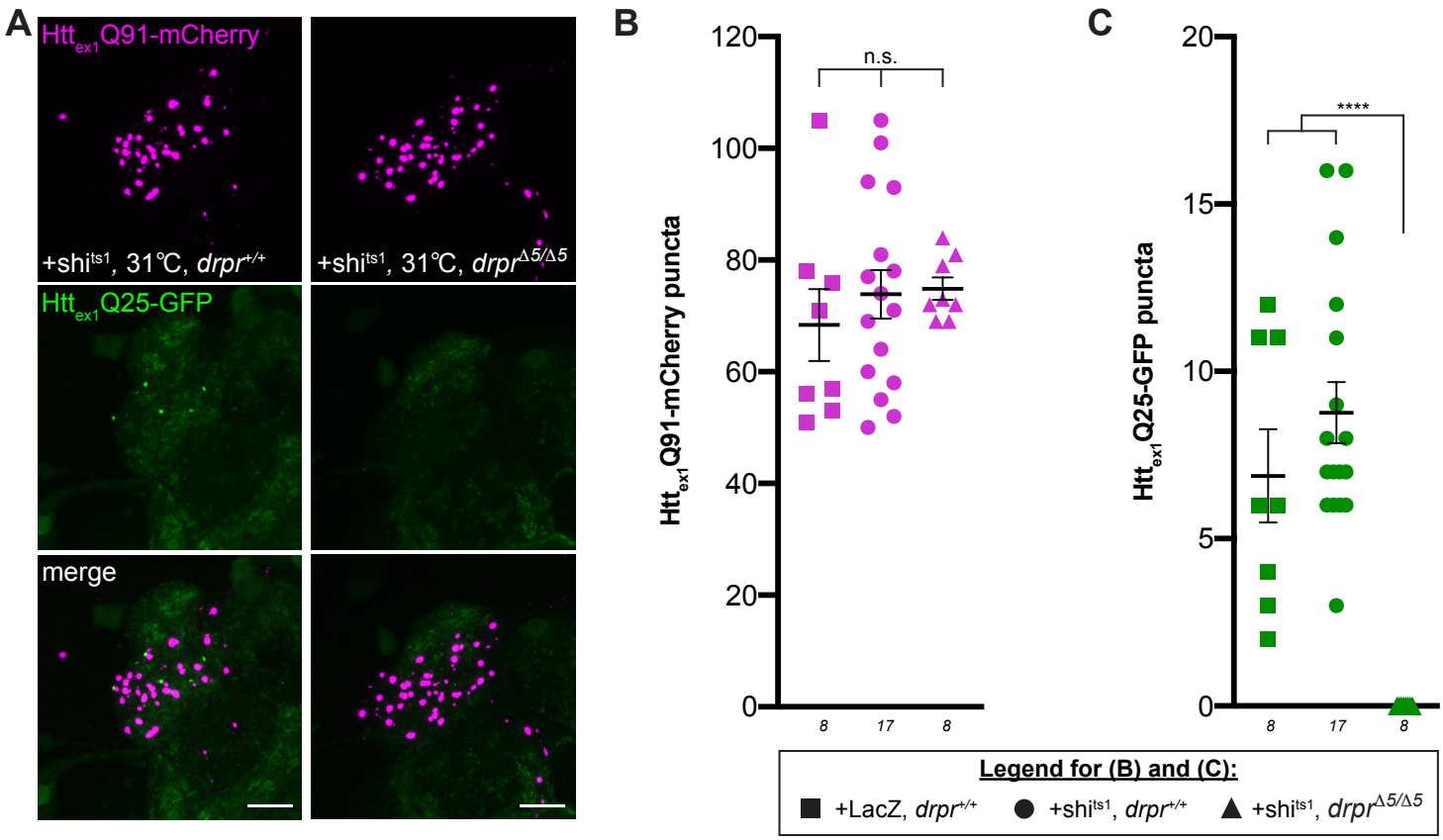

Figure 5 – figure supplement 1. Draper is required for enhanced transfer of mHtt$_{ex1}$ from shi^{ts}-expressing ORNs to synaptically-connected PNs. (A) Maximum-intensity z-projections of the DA1 glomerulus from 7 day-old *drpr*$^{+/+}$ or *drpr*$^{\Delta5/\Delta5}$ adult females co-expressing Htt$_{ex1}$Q91-mCherry with either LacZ or shi^{ts1} in ORNs and Htt$_{ex1}$Q25-GFP in PNs. Adult flies were shifted from 18°C to the restrictive temperature (31°C) upon eclosion. Scale bars = 10 μm. (B and C) Quantification of Htt$_{ex1}$Q91-mCherry (B) and Htt$_{ex1}$Q25-GFP (C) aggregates for controls expressing LacZ in ORNs (*squares*), and flies expressing shi^{ts1} in ORNs in *drpr*$^{+/+}$ (*circles*) or *drpr*$^{\Delta5/\Delta5}$ backgrounds (*triangles*). Horizontal bars indicate means, and error bars indicate ± SEM; *n* is shown below each data set. ****$p < 0.0001$, or n.s. = not significant by one-way ANOVA with Tukey's multiple comparisons tests.

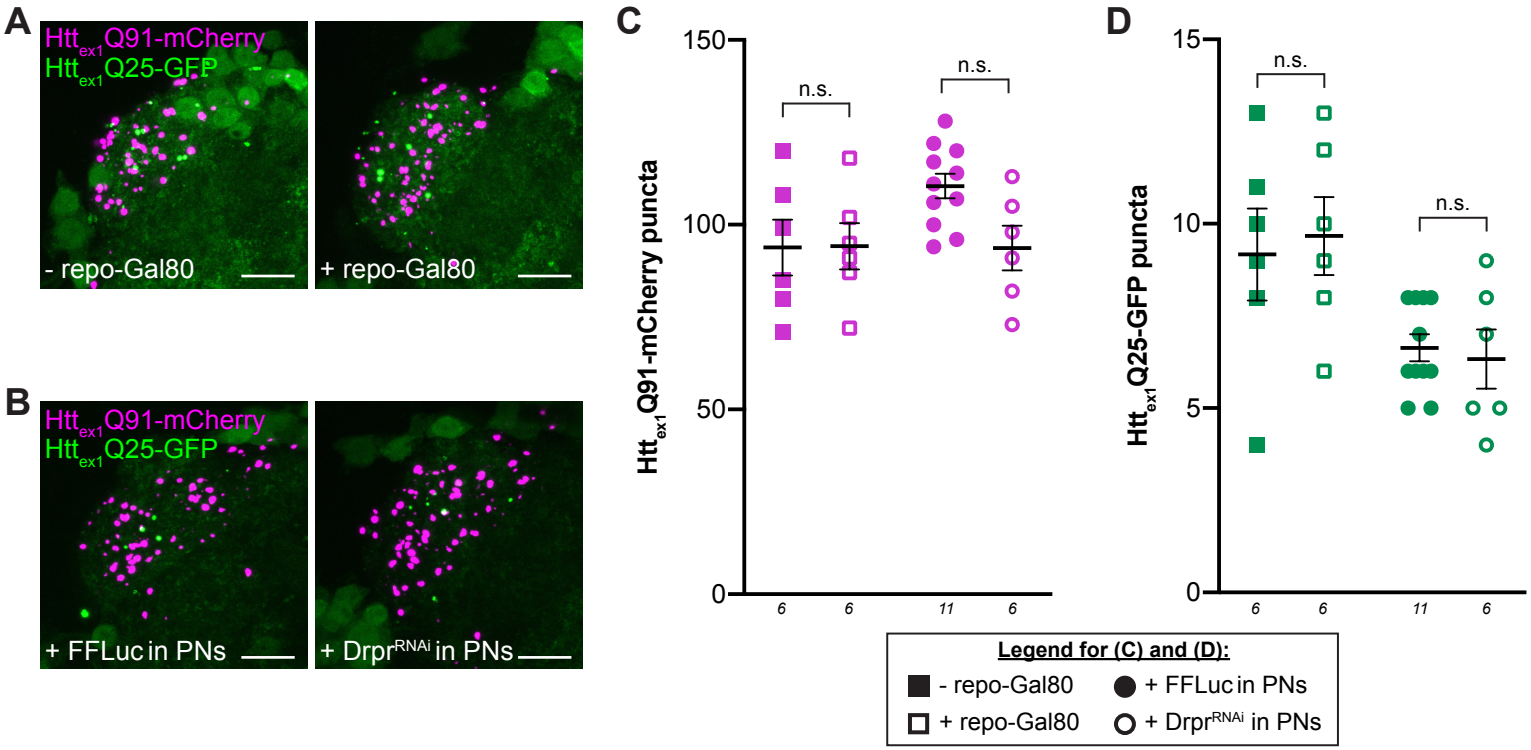

Figure 5 – figure supplement 2. Gal80-mediated repression of Gal4 in glia and RNAi knockdown of *drpr* in PNs do not affect ORN-to-PN transfer of mHtt$_{ex1}$ aggregates. (A and B) Maximum-intensity z-projections of the DA1 glomerulus from 2 week-old adult males showing that (A) inhibiting possible *GH146-Gal4*-mediated expression in glia with *repo-Gal80* or (B) expression of siRNAs targeting *drpr* in PNs do not affect Htt$_{ex1}$Q25-GFP aggregation in PNs when Htt$_{ex1}$Q91-mCherry is expressed in ORNs. Control flies did not express repo-Gal80 (A) or co-expressed firefly luciferase (FFLuc) with Htt$_{ex1}$Q25-GFP in PNs (B). Scale bars = 10 μm. (C and D) Quantification of Htt$_{ex1}$Q91-mCherry (C) and Htt$_{ex1}$Q25-GFP (D) aggregates for genotypes shown in (A) and (B). Horizontal bars indicate mean, and error bars indicate ± SEM; *n* is shown below each data set. n.s. = not significant by one-way ANOVA with Tukey's multiple comparisons tests.

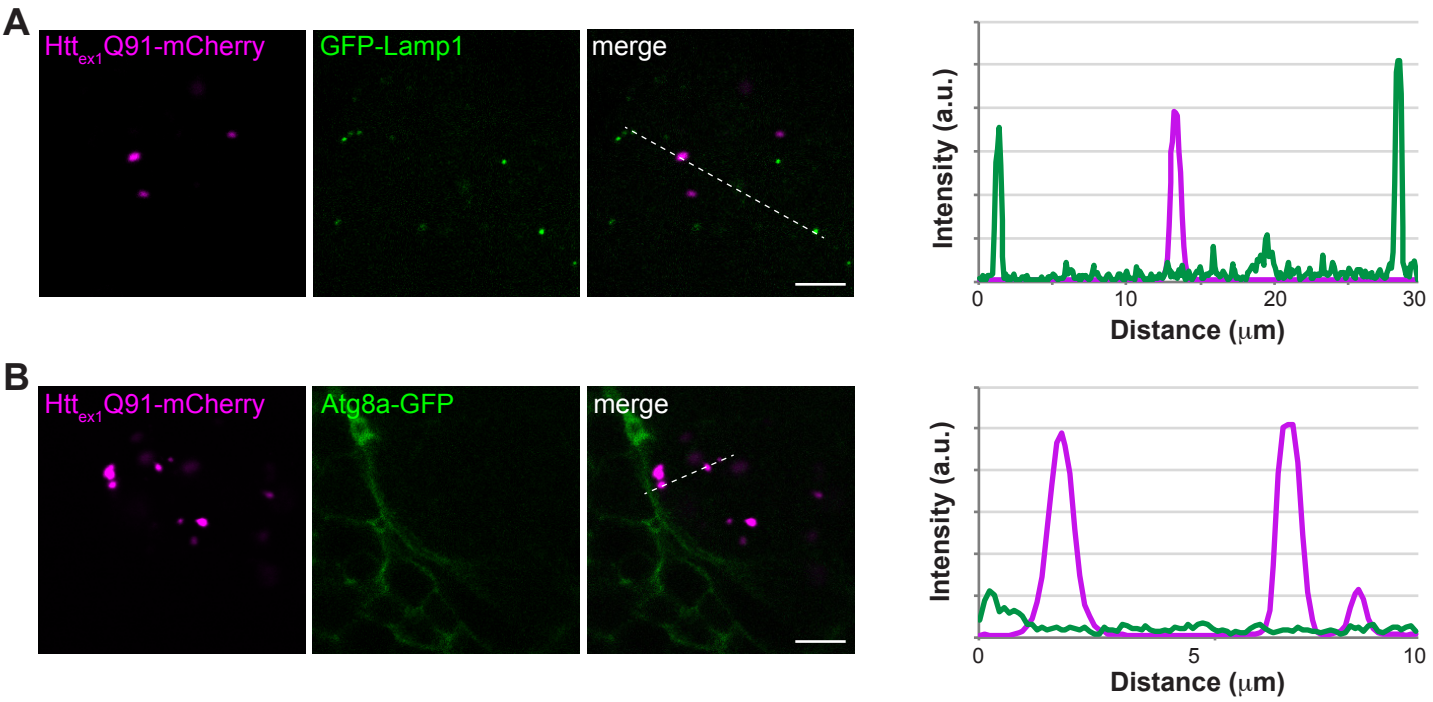

Figure 5 – figure supplement 3. mHtt$_{ex1}$ aggregates generated in ORNs do not co-localize with markers of lysosomes or autophagosomes in glia. (A and B) Single confocal slices from the DA1 glomerulus of 1 week-old adult females expressing Htt$_{ex1}$Q91-mCherry in DA1 ORNs using *Or67d-QF* and the lysosomal marker GFP-Lamp1 (A) or the autophagosome marker Atg8a-GFP (B) in glia using *repo-Gal4*. Line scans in (A) and (B) show intensity of mCherry (*magenta*) and GFP (*green*) fluorescence along dotted lines indicated in images. Scale bars = 5 μm; a.u. = arbitrary units.

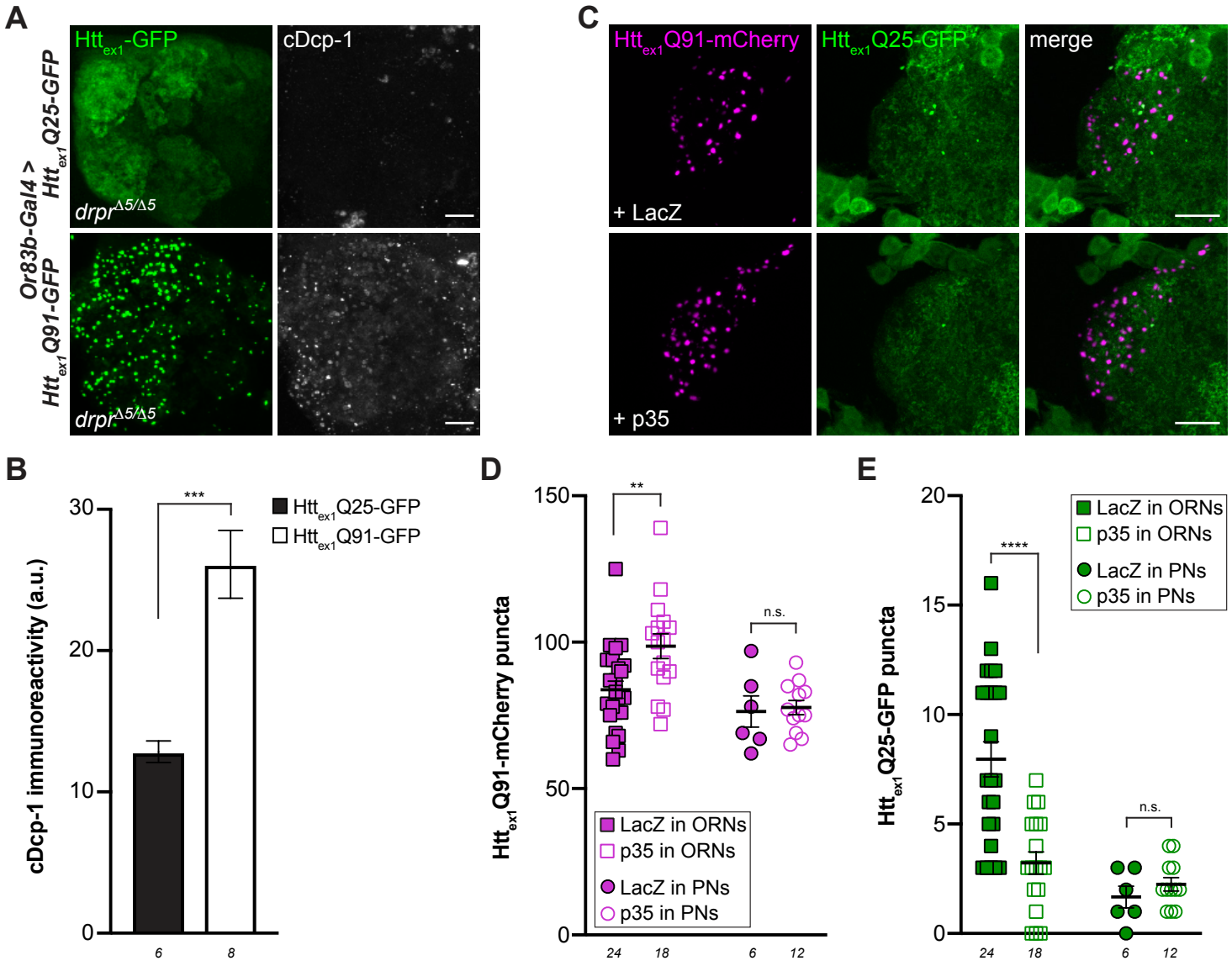

Figure 6. Caspase activity in ORNs mediates mHtt$_{ex1}$ aggregate transfer from ORNs to PNs. (A) Maximum-intensity z-projections of an antennal lobe from 8 day-old *drpr*-null adult males expressing Htt$_{ex1}$Q25-GFP (*top*) or Htt$_{ex1}$Q91-GFP (*bottom*) in most ORNs using *Or83b-Gal4* driver. Brains were immunostained with antibodies against GFP (*green*) or cleaved Dcp-1 (*grayscale*). (B) Quantification of cDcp-1 immunoreactivity in the antennal lobe of flies expressing Htt$_{ex1}$Q25-GFP (*black bar*) or Htt$_{ex1}$Q91-GFP (*white bar*) in Or83b+ ORNs. (C) Maximum-intensity z-projections of the DA1 glomerulus from 12 day-old males co-expressing Htt$_{ex1}$Q91-mCherry with LacZ (control) or p35 in DA1 ORNs and Htt$_{ex1}$Q25-GFP in GH146+ PNs. (D) and (E) Quantification of Htt$_{ex1}$Q91-mCherry (D) or Htt$_{ex1}$Q25-GFP (E) puncta in the DA1 glomerulus of 12 day-old adult males co-expressing Htt$_{ex1}$Q91-mCherry with LacZ or p35 in ORNs (*squares*) or co-expressing Htt$_{ex1}$Q25-GFP with LacZ or p35 in PNs (*circles*). Numbers of aggregates in flies expressing LacZ or p35 are indicated by solid or open shapes, respectively. For quantifications shown in (B), (D), and (E), horizontal bars indicate means and error bars indicate ± SEM; *n* is shown below each data set; **$p < 0.01$, ***$p < 0.001$, or ****$p < 0.0001$ by Student's t-test in (B) or one-way ANOVA with Tukey's multiple comparisons tests in (D) and (E). Scale bars = 10 μm in all images.

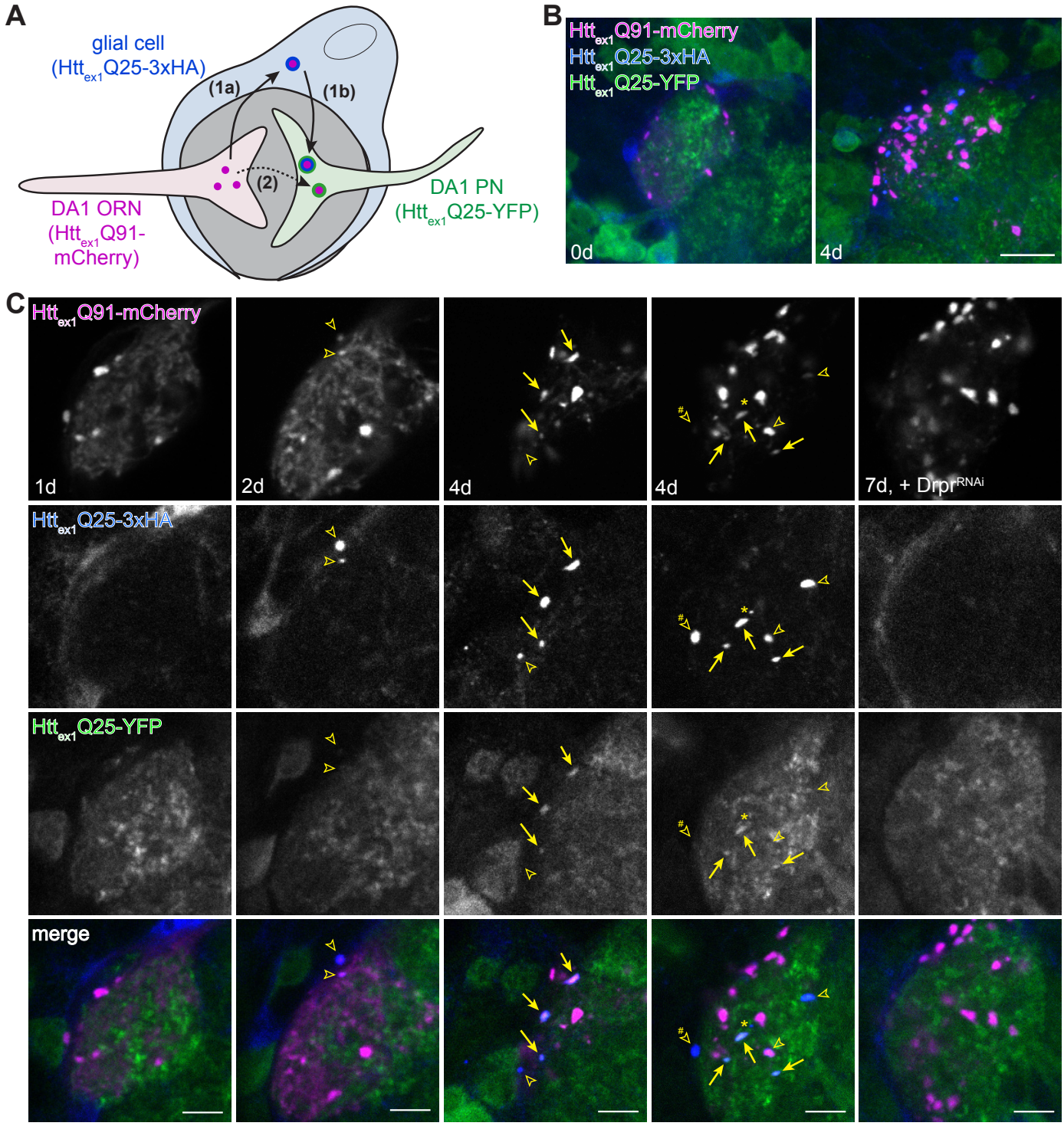
A
glial cell
(Htt$_{ex1}$Q25-3xHA)
(1a)
(1b)
(2)
DA1 ORN
(Htt$_{ex1}$Q91-mCherry)
DA1 PN
(Htt$_{ex1}$Q25-YFP)
B
Htt$_{ex1}$Q91-mCherry
Htt$_{ex1}$Q25-3xHA
Htt$_{ex1}$Q25-YFP
0d
4d
C
Htt$_{ex1}$Q91-mCherry
1d
2d
4d
4d
7d, + Drpr^{RNAi}
Htt$_{ex1}$Q25-3xHA
Htt$_{ex1}$Q25-YFP
merge

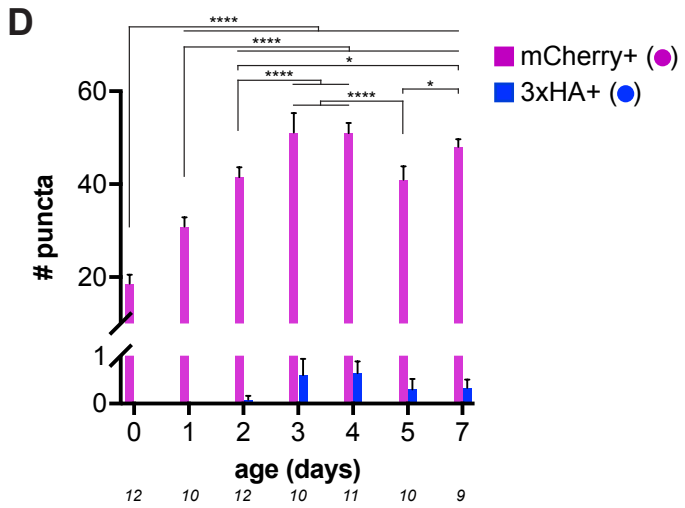
D
mCherry+ (●)
3xHA+ (●)
puncta
age (days)
0 1 2 3 4 5 7
12 10 12 10 11 10 9

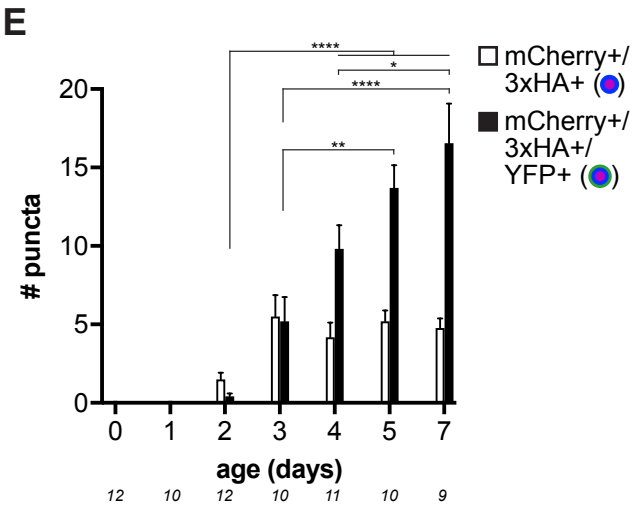
E
mCherry+/ 3xHA+ (●)
mCherry+/ 3xHA+/ YFP+ (●)
puncta
age (days)
0 1 2 3 4 5 7
12 10 12 10 11 10 9

Figure 7. mHtt$_{ex1}$ aggregates transfer from presynaptic ORNs to postsynaptic PNs via a Draper-dependent phagocytic glial cytoplasmic intermediate. (A) Diagram illustrating our experimental approach for testing a role for Draper-dependent glia in Htt$_{ex1}$Q91-mCherry aggregate transfer from DA1 ORNs to DA1 PNs. Flies that combined *Or67d-QF-*, *repo-Gal4-*, and *GH146-LexA:GAD*-driven expression of Htt$_{ex1}$Q91-mCherry in DA1 ORNs, Htt$_{ex1}$Q25-3xHA in all glia, and Htt$_{ex1}$Q25-YFP in ~60% of PNs, respectively, were generated and analyzed for immunoreactivity of each fluorescent protein or epitope tag. If Htt$_{ex1}$Q91-mCherry aggregates travel to PNs via the glial cytoplasm (route 1), triple-labeled (mCherry+/3xHA+/YFP+) aggregates would be expected to appear. By contrast, if Htt$_{ex1}$Q91-mCherry aggregates transfer directly to PNs without accessing the glial cytoplasm (route 2), then only double-labeled (mCherry+/3xHA+ and mCherry+/YFP+) aggregates would be detected. (B) Maximum-intensity z-projections of the DA1 glomerulus from adult females expressing Htt$_{ex1}$Q91-mCherry in DA1 ORNs (*magenta*), Htt$_{ex1}$Q25-3xHA in glia (*blue*), and Htt$_{ex1}$Q25-YFP in PNs (*green*) at the indicated ages. Brains were immunostained with antibodies against the unique mCherry, 3xHA, and GFP tags on each Htt protein. Scale bars = 10 μm. (C) Single confocal z-slices from females with the same genotype as in (B) at the indicated ages. mCherry+/3xHA+/YFP+ aggregates, mCherry+/3xHA+ aggregates, and 3xHA+-only aggregates are indicated by arrows, open arrowheads, and asterisks, respectively. The hashtag in the 7d image indicates an mCherry+/3xHA+ aggregate for which the associated mCherry+ seed is in a different focal plane. Annotations are shown in yellow on each image for increased visibility. Scale bars = 5 μm. (D) and (E) Quantification of aggregates with only one label (D) or co-labeled aggregates (E) that were detected in adult female brains at the indicated ages. Aggregate species that were not detected in our samples (i.e., mCherry+/YFP+ or 3xHA+/YFP+) are not shown. Error bars indicate ± SEM; *n* is shown below each data set. Statistical comparisons were made between different time points for each aggregate species using two-way ANOVA with Tukey's multiple comparisons tests (*$p < 0.05$, *$p < 0.01$, or ****$p < 0.0001$).

Table 1. Genotypes displayed in each figure

Figure panel(s)	Genotype
Figure 1	
C,D,E,F,G	*Or67d-QF,UAS-Htt$_{ex1}$Q25-GFP^{attP3}/(+/Y) ; GH146-Gal4,QUAS-Htt$_{ex1}$Q91-mCherry^{attP24}/+*
H	*Or67d-QF,UAS-Htt$_{ex1}$Q25-GFP^{attP3}/QUAS-RFP-Htt$_{ex1-12}$Q138^{attP3B} ; GH146-Gal4/+*
Figure 1, figure supplement 1	
A	*elav[C155]-Gal4/UAS-Htt$_{ex1}$Q91-mCherry^{attP3}*
B	*elav[C155]-Gal4/+ ; UAS-Htt$_{ex1}$Q25-GFP^{attP24}/+*
C	*elav[C155]-Gal4/UAS-Htt$_{ex1}$Q91-mCherry^{attP3} ; UAS-Htt$_{ex1}$Q25-GFP^{attP24}/+*
D	*elav[C155]-Gal4/UAS-Htt$_{ex1}$Q91-mCherry^{attP3}/+ ; UAS-GFP^{attP24}/+*
Figure 1, figure supplement 2	
A	*Or67d-QF,UAS-Htt$_{ex1}$Q25-GFP^{attP3}/+ ; GH146-Gal4/QUAS-Htt$_{ex1}$Q25-mCherry^{attP24}*
B	*Or67d-QF/Y ; GH146-Gal4,QUAS-Htt$_{ex1}$Q91-mCherry^{attP24}/UAS-GFP^{attP24}*
C	*Or67d-QF,UAS-Htt$_{ex1}$Q25-GFP^{attP3}/QUAS-Gal80 ; GH146-Gal4/QUAS-Htt$_{ex1}$Q91-mCherry^{attP24}*
D	*Or67d-QF,UAS-Htt$_{ex1}$Q25-GFP^{attP3}/+ ; GH146-Gal4/QUAS-Htt$_{ex1}$Q91-mCherry^{attP24} ; UAS-QS/+*
Figure 1, figure supplement 3	
	pebbled-Gal4/QUAS-Htt$_{ex1}$Q91-mCherry^{attP3} ; UAS-Htt$_{ex1}$Q25-GFP^{attP24}/+ ; GH146-QF/+
Figure 2	
A,B,C,D,E,F	*Or67d-QF,UAS-Htt$_{ex1}$Q25-GFP^{attP3}/(+/Y) ; GH146-Gal4,QUAS-Htt$_{ex1}$Q91-mCherry^{attP24}/+*
Figure 3	
A: + LacZ	*Or67d-QF,UAS-Htt$_{ex1}$Q25-GFP^{attP3}/Y ; GH146-Gal4,QUAS-Htt$_{ex1}$Q91-mCherry^{attP24}/+ ; QUAS-nucLacZ/+*
A: + shi^{ts1}	*Or67d-QF,UAS-Htt$_{ex1}$Q25-GFP^{attP3}/Y ; GH146-Gal4,QUAS-Htt$_{ex1}$Q91-mCherry^{attP24}/+; QUAS-shibire^{ts1}#7/+*
B,C: LacZ	*Or67d-QF,UAS-Htt$_{ex1}$Q25-GFP^{attP3}/Y ; GH146-Gal4,QUAS-Htt$_{ex1}$Q91-mCherry^{attP24}/+ ; QUAS-nucLacZ/+*
B,C: shi^{ts1}#1	*Or67d-QF,UAS-Htt$_{ex1}$Q25-GFP^{attP3}/Y ; GH146-Gal4,QUAS-Htt$_{ex1}$Q91-mCherry^{attP24}/+; QUAS-shibire^{ts1}#5/+*
B,C: shi^{ts1}#2	*Or67d-QF,UAS-Htt$_{ex1}$Q25-GFP^{attP3}/Y ; GH146-Gal4,QUAS-Htt$_{ex1}$Q91-mCherry^{attP24}/+; QUAS-shibire^{ts1}#7/+*
D: + LacZ	*Or67d-QF,UAS-Htt$_{ex1}$Q25-GFP^{attP3}/Y ; GH146-Gal4,QUAS-Htt$_{ex1}$Q91-mCherry^{attP24}/+ ; QUAS-nucLacZ/+*
D: + TeTxLC	*Or67d-QF,UAS-Htt$_{ex1}$Q25-GFP^{attP3}/Y ; GH146-Gal4,QUAS-Htt$_{ex1}$Q91-mCherry^{attP24}/Pin; QUAS-TeTxLC#9c/+*
E,F: LacZ	*Or67d-QF,UAS-Htt$_{ex1}$Q25-GFP^{attP3}/Y ; GH146-Gal4,QUAS-Htt$_{ex1}$Q91-mCherry^{attP24}/+ ; QUAS-nucLacZ/+*

E,F: TeTxLC#1	*Or67d-QF,UAS-Htt$_{ex1}$Q25-GFP^{attP3}/Y ; GH146-Gal4,QUAS-Htt$_{ex1}$Q91-mCherry^{attP24}/QUAS-TeTxLC#4c ; +/(Dh/Tm6b)*
E,F: TeTxLC#2	*Or67d-QF,UAS-Htt$_{ex1}$Q25-GFP^{attP3}/Y ; GH146-Gal4,QUAS-Htt$_{ex1}$Q91-mCherry^{attP24}/Pin; QUAS-TeTxLC#9c/+*
G: + LacZ	*Or67d-QF,UAS-Htt$_{ex1}$Q25-GFP^{attP3}/+ ; GH146-Gal4,QUAS-Htt$_{ex1}$Q91-mCherry^{attP24}/+ ; QUAS-nucLacZ/+*
G: + dTrpA	*Or67d-QF,UAS-Htt$_{ex1}$Q25-GFP^{attP3}/+ ; GH146-Gal4,QUAS-Htt$_{ex1}$Q91-mCherry^{attP24}/QUAS-dTrpA#7*
H,I: LacZ	*Or67d-QF,UAS-Htt$_{ex1}$Q25-GFP^{attP3}/+ ; GH146-Gal4,QUAS-Htt$_{ex1}$Q91-mCherry^{attP24}/+ ; QUAS-nucLacZ/+*
H,I: dTrpA#1	*Or67d-QF,UAS-Htt$_{ex1}$Q25-GFP^{attP3}/+ ; GH146-Gal4,QUAS-Htt$_{ex1}$Q91-mCherry^{attP24}/QUAS-dTrpA#7*
H,I: dTrpA#2	*Or67d-QF,UAS-Htt$_{ex1}$Q25-GFP^{attP3}/QUAS-dTrpA#5 ; GH146-Gal4,QUAS-Htt$_{ex1}$Q91-mCherry^{attP24}/+*
H,I: dTrpA#3	*Or67d-QF,UAS-Htt$_{ex1}$Q25-GFP^{attP3}/+ ; GH146-Gal4,QUAS-Htt$_{ex1}$Q91-mCherry^{attP24}/+ ; QUAS-dTrpA#6/+*
Figure 4	
A,B,C: + LacZ	*Or67d-QF,QUAS-Htt$_{ex1}$Q91-mCherry^{attP3}/+ ; QUAS-mCD8-GFP/+ ; QUAS-nucLacZ/+*
A,B,C: + shi^{ts1}	*Or67d-QF,QUAS-Htt$_{ex1}$Q91-mCherry^{attP3}/+ ; QUAS-mCD8-GFP/+ ; QUAS-shibire^{ts1}#7/+*
D: + LacZ	*Or67d-QF,QUAS-Htt$_{ex1}$Q91-mCherry^{attP3}/Y ; UAS-Htt$_{ex1}$Q25-YFP^{attP24}/+ ; repo-Gal4/QUAS-nucLacZ*
D: + shi^{ts1}	*Or67d-QF,QUAS-Htt$_{ex1}$Q91-mCherry^{attP3}/Y ; UAS-Htt$_{ex1}$Q25-YFP^{attP24}/+ ; repo-Gal4/QUAS-shibire^{ts1}#7*
E,F: LacZ	*Or67d-QF,QUAS-Htt$_{ex1}$Q91-mCherry^{attP3}/Y ; UAS-Htt$_{ex1}$Q25-YFP^{attP24}/+ ; repo-Gal4/QUAS-nucLacZ*
E,F: shi^{ts1}#1	*Or67d-QF,QUAS-Htt$_{ex1}$Q91-mCherry^{attP3}/Y ; UAS-Htt$_{ex1}$Q25-YFP^{attP24}/+ ; repo-Gal4/QUAS-shibire^{ts1}#5*
E,F: shi^{ts1}#2	*Or67d-QF,QUAS-Htt$_{ex1}$Q91-mCherry^{attP3}/Y ; UAS-Htt$_{ex1}$Q25-YFP^{attP24}/+ ; repo-Gal4/QUAS-shibire^{ts1}#7*
Figure 5	
A,B,C: *drpr$^{\Delta 5/+}$*	*Or67d-QF,UAS-Htt$_{ex1}$Q25-GFP^{attP3}/(+/Y) ; GH146-Gal4,QUAS-Htt$_{ex1}$Q91-mCherry^{attP24}/+ ; drpr$^{\Delta 5}$/+*
A,B,C: *drpr$^{\Delta 5/\Delta 5}$*	*Or67d-QF,UAS-Htt$_{ex1}$Q25-GFP^{attP3}/(+/Y) ; GH146-Gal4,QUAS-Htt$_{ex1}$Q91-mCherry^{attP24}/+ ; drpr$^{\Delta 5}$/drpr$^{\Delta 5}$*
D,E: *drpr$^{+/+}$*	*Or67d-QF,QUAS-Htt$_{ex1}$Q91-mCherry^{attP3}/(+/Y)*
D,E: *drpr$^{\Delta 5/\Delta 5}$*	*Or67d-QF,QUAS-Htt$_{ex1}$Q91-mCherry^{attP3}/(+/Y) ; ; drpr$^{\Delta 5}$/drpr$^{\Delta 5}$*
Figure 5, figure supplement 1	
A,B,C: + shi^{ts1}, *drpr$^{+/+}$*	*Or67d-QF,UAS-Htt$_{ex1}$Q25-GFP^{attP3}/QUAS-shibire^{ts1}#2 ; GH146-Gal4,QUAS-Htt$_{ex1}$Q91-mCherry^{attP24}/+*
A,B,C: + shi^{ts1}, *drpr$^{\Delta 5/\Delta 5}$*	*Or67d-QF,UAS-Htt$_{ex1}$Q25-GFP^{attP3}/QUAS-shibire^{ts1}#2 ; GH146-Gal4,QUAS-Htt$_{ex1}$Q91-mCherry^{attP24}/+ ; drpr$^{\Delta 5}$/drpr$^{\Delta 5}$*
B,C: + LacZ, *drpr$^{+/+}$*	*Or67d-QF,UAS-Htt$_{ex1}$Q25-GFP^{attP3}/+ ; GH146-Gal4,QUAS-Htt$_{ex1}$Q91-mCherry^{attP24}/+ ; QUAS-nucLacZ/+*

Figure 5, figure supplement 2	
A,C,D: - repo-Gal80	*Or67d-QF,UAS-Htt$_{ex1}$Q25-GFP^{attP3}/Y ; GH146-Gal4,QUAS-Htt$_{ex1}$Q91-mCherry^{attP24}/+*
A,C,D: + repo-Gal80	*Or67d-QF,UAS-Htt$_{ex1}$Q25-GFP^{attP3}/Y ; GH146-Gal4,QUAS-Htt$_{ex1}$Q91-mCherry^{attP24}/repo-Gal80*
B,C,D: + FFLuc in PNs	*Or67d-QF,UAS-Htt$_{ex1}$Q25-GFP^{attP3}/Y ; GH146-Gal4,QUAS-Htt$_{ex1}$Q91-mCherry^{attP24}/+ ; UAS-FFLuc^{attP2}/+*
B,C,D: + Draper^{RNAi} in PNs	*Or67d-QF,UAS-Htt$_{ex1}$Q25-GFP^{attP3}/Y ; GH146-Gal4,QUAS-Htt$_{ex1}$Q91-mCherry^{attP24}/+ ; UAS-Draper$^{RNAi\#5}$/+*
Figure 5, figure supplement 3	
A	*Or67d-QF,QUAS-Htt$_{ex1}$Q91-mCherry^{attP3}/+ ; UAS-GFP-Lamp1/+ ; repo-Gal4/+*
B	*Or67d-QF,QUAS-Htt$_{ex1}$Q91-mCherry^{attP3}/+ ; UAS-Atg8a-GFP/+ ; repo-Gal4/+*
Figure 6	
A(top),B	*Or83b-Gal4,UAS-Htt$_{ex1}$Q25-GFP^{attP24}/+ ; drpr$^{\Delta 5}$/drpr$^{\Delta 5}$*
A(bottom),B	*Or83b-Gal4,UAS-Htt$_{ex1}$Q91-GFP^{attP24}/+ ; drpr$^{\Delta 5}$/drpr$^{\Delta 5}$*
C: + LacZ	*Or67d-QF,UAS-Htt$_{ex1}$Q25-GFP^{attP3}/Y ; GH146-Gal4,QUAS-Htt$_{ex1}$Q91-mCherry^{attP24}/+ ; QUAS-nucLacZ/+*
C: + p35	*Or67d-QF,UAS-Htt$_{ex1}$Q25-GFP^{attP3}/Y ; GH146-Gal4,QUAS-Htt$_{ex1}$Q91-mCherry^{attP24}/+; QUAS-p35/+*
D,E: LacZ in ORNs	*Or67d-QF,UAS-Htt$_{ex1}$Q25-GFP^{attP3}/Y ; GH146-Gal4,QUAS-Htt$_{ex1}$Q91-mCherry^{attP24}/+ ; QUAS-nucLacZ/+*
D,E: p35 in ORNs	*Or67d-QF,UAS-Htt$_{ex1}$Q25-GFP^{attP3}/Y ; GH146-Gal4,QUAS-Htt$_{ex1}$Q91-mCherry^{attP24}/+; QUAS-p35/+*
D,E: LacZ in PNs	*Or67d-QF,UAS-Htt$_{ex1}$Q25-GFP^{attP3}/Y ; GH146-Gal4,QUAS-Htt$_{ex1}$Q91-mCherry^{attP24}/UAS-LacZ*
D,E: p35 in PNs	*Or67d-QF,UAS-Htt$_{ex1}$Q25-GFP^{attP3}/Y ; GH146-Gal4,QUAS-Htt$_{ex1}$Q91-mCherry^{attP24}/UAS-p35*
Figure 7	
B,C,D,E	*Or67d-QF,QUAS-Htt$_{ex1}$Q91-mCherry^{attP3}/+ ; GH146-LexA::GAD,LexAop-Htt$_{ex1}$Q25-YFP^{attP24}/UAS-Htt$_{ex1}$Q25-3xHA^{attP24} ; repo-Gal4/+*
C: + Drpr^{RNAi}	*Or67d-QF,QUAS-Htt$_{ex1}$Q91-mCherry^{attP3}/+ ; GH146-LexA::GAD,LexAop-Htt$_{ex1}$Q25-YFP^{attP24}/UAS-Htt$_{ex1}$Q25-3xHA^{attP24} ; repo-Gal4/UAS-Draper$^{RNAi\#5}$*